

Ligand recognition and allosteric modulation of the human MRGPRX1 receptor

Received: 23 May 2022

Accepted: 13 September 2022

Published online: 27 October 2022

 Check for updates


Yongfeng Liu ^{1,2,7}, Can Cao ^{1,7}, Xi-Ping Huang^{1,2}, Ryan H. Gumpfer¹, Moira M. Rachman³, Sheng-Luen Shih ^{1,2}, Brian E. Krumm ¹, Shicheng Zhang ¹, Brian K. Shoichet ³, Jonathan F. Fay ^{4,6}  and Bryan L. Roth ^{1,2,5} 

The human MAS-related G protein-coupled receptor X1 (MRGPRX1) is preferentially expressed in the small-diameter primary sensory neurons and involved in the mediation of nociception and pruritus. Central activation of MRGPRX1 by the endogenous opioid peptide fragment BAM8-22 and its positive allosteric modulator ML382 has been shown to effectively inhibit persistent pain, making MRGPRX1 a promising target for non-opioid pain treatment. However, the activation mechanism of MRGPRX1 is still largely unknown. Here we report three high-resolution cryogenic electron microscopy structures of MRGPRX1–Gαq in complex with BAM8-22 alone, with BAM8-22 and ML382 simultaneously as well as with a synthetic agonist compound-16. These structures reveal the agonist binding mode for MRGPRX1 and illuminate the structural requirements for positive allosteric modulation. Collectively, our findings provide a molecular understanding of the activation and allosteric modulation of the MRGPRX1 receptor, which could facilitate the structure-based design of non-opioid pain-relieving drugs.

Itch and pain are generally recognized as two distinct and frequently unpleasant sensations^{1,2} that markedly affect quality of life³. Typically, the sensation of itch evokes scratching, whereas pain stimuli elicit withdrawal⁴. Although their behavioral responses are different, the sensations of itch and pain share overlapping mediators and receptors⁵. For example, many membrane proteins that have been implicated in the mediation of itch transduction, including histamine receptors⁶, Mas-related G protein-coupled receptors (MRGPRs)⁷, protease-activated receptors (PARs)⁸ and ion channels⁹, also play key roles in the pain signaling pathway.

MRGPRs represent a subset of G protein-coupled receptors (GPCRs) comprising more than 50 members in human and rodents¹⁰. Among these, MRGPRX1 has gained increasing interest because of its emerging roles in the regulation of both pruritus and chronic pain^{11,12}.

The activation of MRGPRX1 has dual roles: the peripheral activation of MRGPRX1 elicits itch, and its central activation may dampen pain¹². A variety of endogenous enkephalin fragments, including bovine adrenal medulla (BAM) peptide 8-22, have been shown to activate MRGPRX1 via the Gαq/11 signaling pathway¹³. A positive allosteric modulator (PAM), ML382, has been reported to further enhance the activation of MRGPRX1 by BAM8-22 at the central terminals to prevent pain signals passing to spinal cord neurons, thus effectively attenuating spinal nociceptive transmission^{12,14}. Moreover, MRGPRX1 expression is largely restricted to the sensory neurons of dorsal root ganglion^{13,15}, which makes it a potentially ideal non-opioid pain target that may avoid the addiction and respiratory depression adverse effects caused by the activation of opioid receptors in the central nervous system.

¹Department of Pharmacology, University of North Carolina School of Medicine, Chapel Hill, NC, USA. ²National Institute of Mental Health Psychoactive Drug Screening Program, University of North Carolina School of Medicine, Chapel Hill, NC, USA. ³Department of Pharmaceutical Sciences, University of California, San Francisco School of Medicine, San Francisco, CA, USA. ⁴Department of Biochemistry and Biophysics, University of North Carolina School of Medicine, Chapel Hill, NC, USA. ⁵Division of Chemical Biology and Medicinal Chemistry, University of North Carolina School of Medicine, Chapel Hill, NC, USA. ⁶Present address: Department of Biochemistry and Molecular Biology, University of Maryland School of Medicine, Baltimore, MD, USA. ⁷These authors contributed equally: Yongfeng Liu, Can Cao.  e-mail: fayj@unc.edu; bryan_roth@med.unc.edu

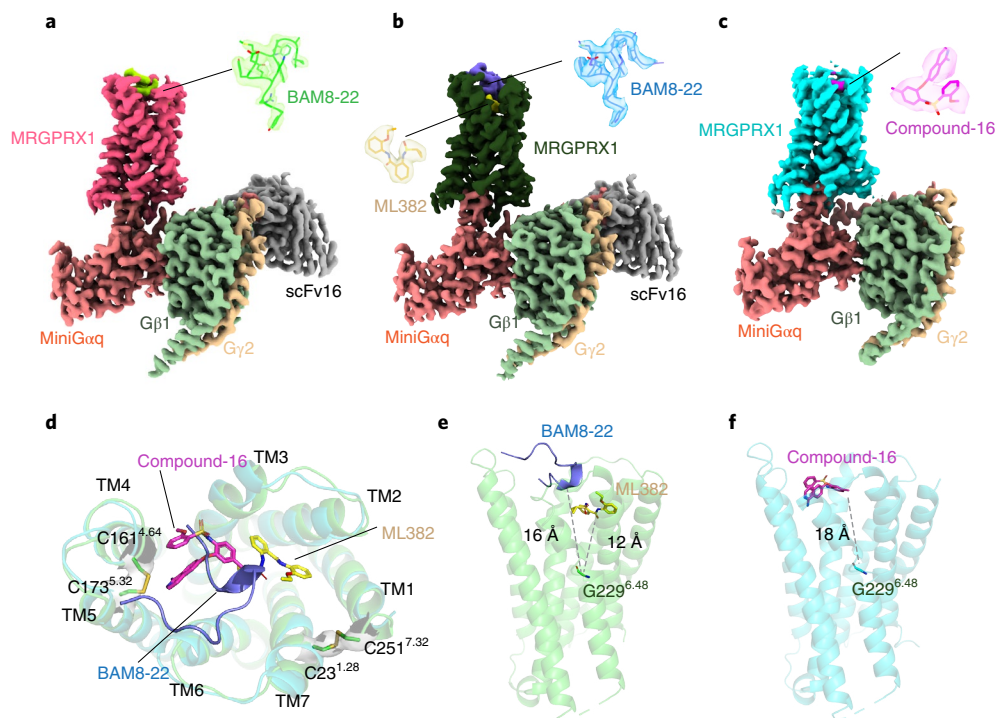


Fig. 1 | Cryo-EM structures of MRGPRX1–Gq complexes. **a–c**, Cryo-EM density maps of MRGPRX1–Gq in complex with BAM8-22 (**a**), BAM8-22/ML382 (**b**) and compound-16 (**c**). **d**, Structure superposition of MRGPRX1–Gq–BAM8-22/ML382 complex with MRGPRX1–Gq–compound-16 complex, highlighting the overall binding sites of BAM8-22, ML382 and compound-16. The peptide agonist

BAM8-22 is shown as a cartoon. The small-molecule ligands and disulfide bonds are shown as sticks. **e**, BAM8-22 and ML382 bind to the extracellular surface far away from G^{6.48} in the MRGPRX1–Gq–BAM8-22/ML382. **f**, Compound-16 binds to the extracellular orthosteric pocket far away from G^{6.48} in MRGPRX1–Gq–compound-16.

However, the lack of structural information limits understanding of the activation and allosteric regulatory mechanisms of MRGPRX1, which impedes the structure-based discovery of drugs targeting MRGPRX1. In our recent studies, we determined the cryogenic electron microscopy (cryo-EM) structures of MRGPRX2 and MRGPRX4 with their cognate G protein complexes and discovered novel small-molecule tools that could accelerate their functional study¹⁶. The structures of MRGPRX2 and MRGPRX4 reveal a shallow binding mode of MRGPR agonists and highlight the important role of two conserved acids residues—that is, D^{5.36} and E^{4.60}—in the determination of charged agonist recognition. In this study, we determined three structures of MRGPRX1–Gαq in complex with a synthetic small-molecule agonist compound-16 (ref. ¹⁷), peptide agonist BAM8-22 alone and BAM8-22 in presence with ML382, respectively. The orthosteric binding pocket of MRGPRX1 diverges considerably from MRGPRX2 and MRGPRX4, although their transducer interfaces are nearly identical. Moreover, the structures also reveal that PAM ML382 may exert its action by directly interacting with BAM8-22. Collectively, our structural and biochemical analyses provide important mechanistic insights for the activation and allosteric modulation mechanism of MRGPRX1, which will accelerate the structure-based drug discovery of the MRGPRX1 receptor and provide new therapeutic opportunities for non-opioid analgesics.

Results

Cryo-EM structures of MRGPRX1–Gq complexes

For structural studies, we assembled MRGPRX1 receptor–Gq complexes by co-expression of the receptor with our previously reported mini-Gq heterotrimer construct¹⁸ and further incubated with G protein–stabilizing antibody scFv16 (ref. ¹⁹). The structures of MRGPRX1–Gq–BAM8-22 complexes with and without the PAM ML382 were determined at 2.7 Å and 2.9 Å (Fig. 1a,b, Extended Data Fig. 1 and Supplementary Figs. 1 and 2), respectively. In addition, the structure of the MRGPRX1–Gq

complex bound to the small-molecule orthosteric agonist compound-16 was determined at a global resolution of 3.25 Å in the absence of scFv16 (Fig. 1c, Extended Data Fig. 1 and Supplementary Figs. 1 and 2). These relatively high-resolution density maps of the three complexes enabled us to unambiguously model most portions of the MRGPRX1 receptor, the mini-Gq heterotrimer, scFv16 and the bound ligands (Extended Data Fig. 2). Most of the sidechains in the transmembrane helices (TM1–TM7) of MRGPRX1 were well-defined, whereas the N-terminus and C-terminus and ICL3 of the receptor were poorly observed and not modeled.

The overall structure of MRGPRX1 shares a similar conformation with MRGPRX2 and MRGPRX4 (ref. ¹⁶). Like MRGPRX2, MRGPRX1 also has a wide-open pocket that can be further divided into two sub-pockets: the orthosteric pocket formed by TM3–TM6 and the allosteric pocket formed by TM1–TM3, TM6 and TM7. The agonists compound-16 and BAM8-22 bind into the presumed orthosteric pocket, whereas ML382 binds into the allosteric pocket at a position near the endogenous agonist BAM8-22 (Fig. 1d). Both the agonists and the PAM bind to MRGPRX1 at the very extracellular side that is over 10 Å away from the residue G^{6.48} (superscript denoted as Ballesteros–Weinstein number²⁰), displaying a shallow binding mode (Fig. 1e,f). Besides the previously characterized TM4–TM5 disulfide bond seen in MRGPRX2 and MRGPRX4, we also observed a TM1–TM7 disulfide bond between C23^{1.28} and C251^{7.32} in the ML382-bound MRGPRX1 structure (Fig. 1d). As MRGPRs lack the canonical TM3–ECL2 disulfide bond, these unique disulfide bonds might be important for the structure and signaling integrity of MRGPRs.

Orthosteric agonist binding mode of BAM8-22

BAM8-22 is a C-terminal fragment of the opioid peptide BAM, which lacks the met-enkephalin motif (YGGFM) for opioid binding¹³. In the structure of the MRGPRX1–Gq–BAM8-22 complex, the endogenous

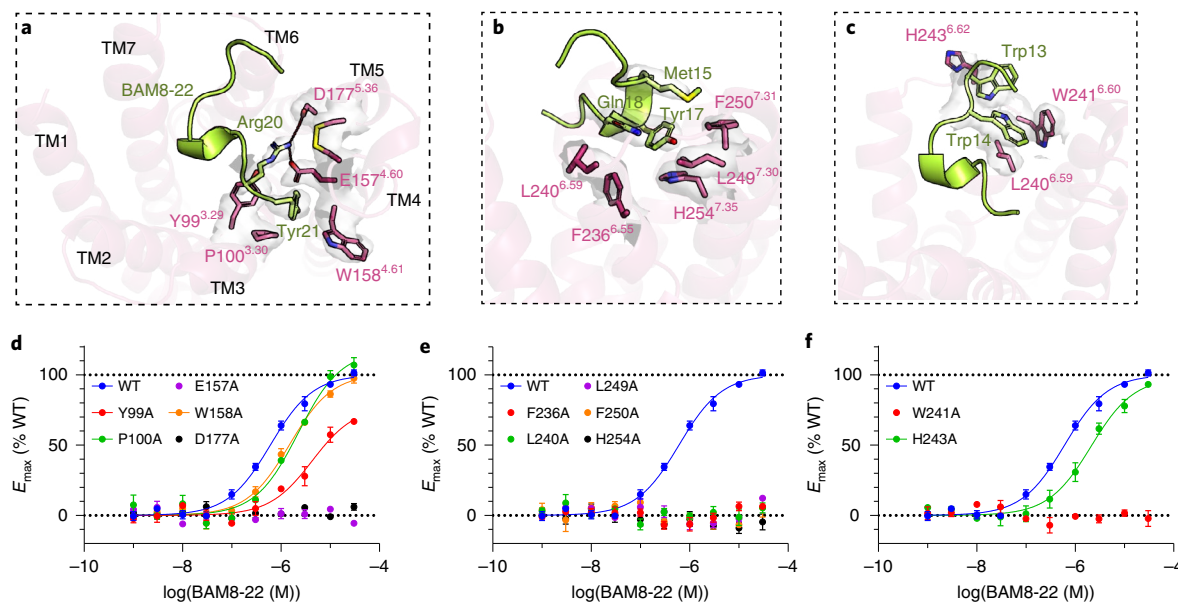


Fig. 2 | Interactions of the endogenous peptide agonist BAM8-22 with MRGPRX1. **a–c**, Key interactions between MRGPRX1 and the C-terminus (**a**), middle part (**b**) and N-terminus (**c**) of BAM8-22. Hydrogen bonds are shown as red dashed lines. **d–f**, Alanine substitution of key MRGPRX1 residues interacting

with the C-terminus (**d**), middle part (**e**) and N-terminus (**f**) of BAM8-22 reduced BAM8-22-stimulated Gq activation by BRET2. Data are presented as mean \pm s.e.m. of three biological replicates. E_{max} , maximum effect; WT, wild-type.

peptide agonist BAM8-22 extends over the orthosteric pocket with a U-shaped hairpin binding pose (Fig. 2a). Specifically, the C-terminal residue Arg20 of BAM8-22 binds into the negatively charged orthosteric pocket and forms strong charge interactions with two acidic residues, D177^{5,36} and E157^{4,60} (Fig. 2a). Similar charge interactions are also observed in MRGPRX2 (ref. 16), indicating that these two exposed acidic residues are crucial for the ligand recognition and activation of both MRGPRX1 and MRGPRX2. In addition, Tyr21 of BAM8-22 inserts deeply into a side cavity formed by Y99^{3,29}, P100^{3,30}, E157^{4,60} and W158^{4,61} (Fig. 2a), thereby restricting the peptide C-terminus. As Arg20 and Tyr21 directly bind into the orthosteric pocket, these two C-terminal residues may be the key motif of BAM8-22 peptide responsible for receptor activation. This might also explain a previous observation that a variety of FR-amide peptides, which have similar C-terminal residues like Arg20–Tyr21 (RY) of BAM8-22, could also activate the mouse analog of MRGPRX1 (ref. 21). The middle portion (Met15–Gln18) and the N-terminus (Trp13–Trp14) of BAM8-22 extends along the interface between orthosteric and allosteric pockets and forms mainly hydrophobic interactions with surrounding residues, including F236^{6,55}, L240^{6,59}, W241^{6,60}, H243^{6,62}, L249^{7,30}, F250^{7,31} and H254^{7,35}, in TM6, TM7 and ECL3 (Fig. 2b,c). By contrast, the remaining N-terminus of BAM8-22 extended into the extracellular solvent and is not directly involved in peptide binding (Fig. 2a–c), which explains the previous observation that deletion of the first few residues of the BAM peptide does not affect its potency at MRGPRX1 (ref. 13).

We then used our recently developed bioluminescence resonance energy transfer assay 2 (BRET2)-based G α q–G β γ dissociation assay²² to examine BAM8-22-stimulated MRGPRX1 signaling in response to the individual pocket mutations (Fig. 2d–f and Supplementary Table 1). As expected, the neutralizing mutations of the negatively charged residues D177^{5,36}A and E157^{4,60}A completely abolished the activity of BAM8-22 (Fig. 2d). Surprisingly, removal of the hydrophobic moieties from F236^{6,55}, L240^{6,59}, W241^{6,60}, L249^{7,30}, F250^{7,31} and H254^{7,35} by alanine substitution also abolishes BAM8-22-stimulated receptor activation (Fig. 2e,f), suggesting that BAM8-22-stimulated MRGPRX1 signaling requires a well-defined pocket shape. Apparently, the activation of MRGPRX1 is also mediated by the critical charge interactions between the positively charged Arg20 of BAM8-22 and the two conserved acidic

residues, D177^{5,36} and E157^{4,60}, of MRGPRX1. However, MRGPRX1 does not have a ‘sidechain-only’ narrow orthosteric pocket seen in MRGPRX2 (ref. 16), thus it cannot promiscuously respond to basic peptides. Indeed, BAM8-22 requires a strict peptide sequence to position Arg20 toward the acidic residues D177^{5,36} and E157^{4,60} for receptor activation as several N-terminal truncations of BAM8-22, such as BAM15-22 and BAM18-22, greatly decrease the peptide-stimulated activation of MRGPRX1 (ref. 13).

Unique allosteric modulation mode of MRGPRX1 by ML382

To date, diverse allosteric binding sites have been reported from the crystal or cryo-EM structures of class A GPCRs^{23–26} (Extended Data Fig. 3). In our structure of MRGPRX1 bound to BAM8-22 and ML382, the PAM molecule ML382 binds at the extracellular side of the MRGPRX1 (Fig. 3a). In general, ML382 positions next to the orthosteric agonist BAM8-22 and engages an allosteric pocket with extensive electrostatic and hydrophobic interactions with TM1–TM3, TM6 and TM7 (Figs. 1d and 3a). Structurally, ML382 is a ‘bicycle’-like molecule composed of three chemical groups: benzamide core scaffold, cyclopropyl sulfonamide group and 2-ethoxyphenyl group. The oxygen atoms of both the cyclopropyl sulfonamide and the benzamide groups in the middle part of ML382 form hydrogen bonds with the basic residues R79^{2,57} and H254^{7,35} of MRGPRX1 (Fig. 3b). The two aromatic ‘wheels’ of ML382 interact with the receptor mainly through hydrophobic interactions with the surrounding residues (Fig. 3b,c). Mutagenesis studies reveal that Y82^{2,60} and I258^{7,39}, which sandwich the ML382 molecule, greatly reduced the ML382-induced PAM signaling, suggesting that these two residues might be critical for the PAM activity of ML382 (Fig. 3d, Extended Data Fig. 4 and Supplementary Table 2). Intriguingly, R79^{2,57}A, which is 10 Å from the peptide binding site, also abolished the BAM8-22-stimulated MRGPRX1 activation (Fig. 3d), suggesting that the alanine substitution of this distal allosteric pocket residue indirectly affects its signaling. More importantly, the upper part of 2-ethoxyphenyl and cyclopropyl sulfonamide groups of ML382 also form hydrophobic interactions with the Tyr17 of BAM8-22 (Fig. 3c and Supplementary Fig. 3). A previous structural activity relationship (SAR) study of ML382 showed that substitution of the cyclopropyl group of ML382 with large moieties resulted in loss of PAM activity¹⁴. Because

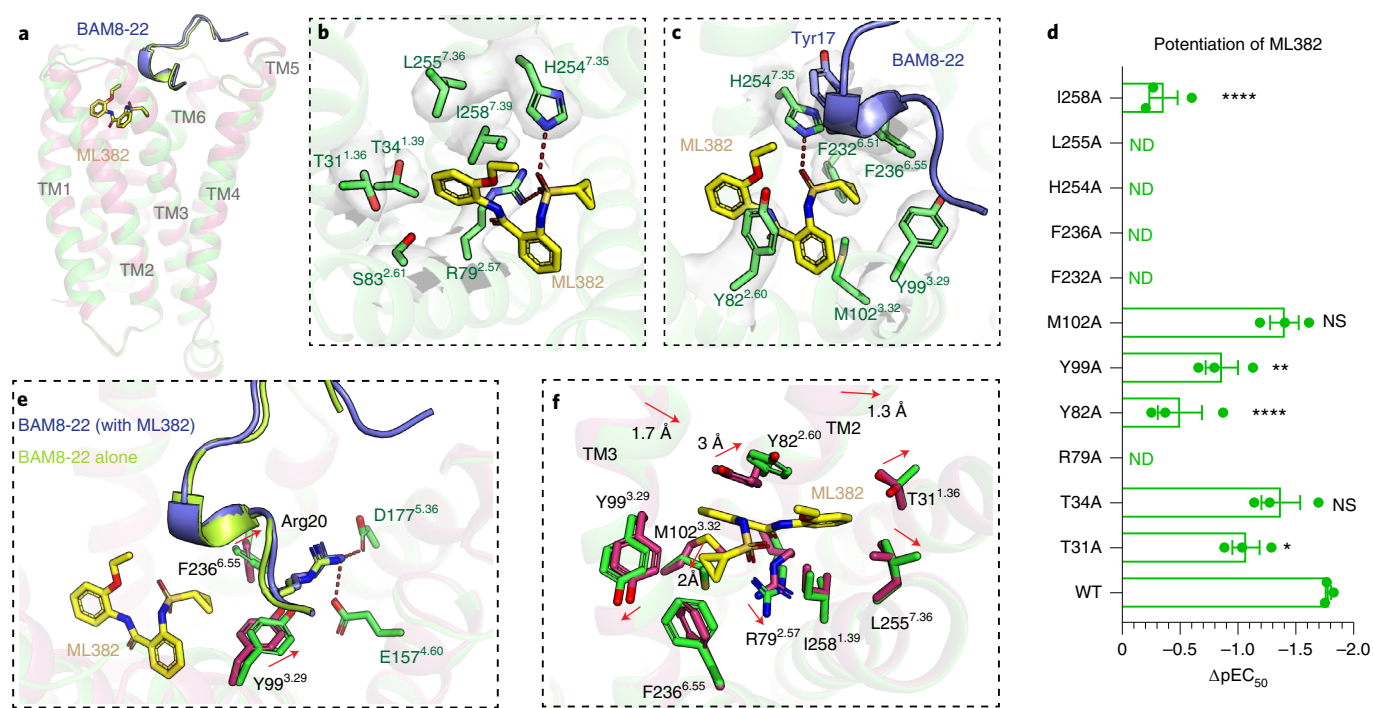


Fig. 3 | Structural basis for ML382 modulation. **a**, Structural comparison of MRGPRX1–BAM8-22 (red) complex with MRGPRX1–BAM8-22/ML382 (green) complex, highlighting the overall binding mode of BAM8-22 and ML382. The peptide BAM8-22 is colored by limon and blue, respectively. The allosteric ligand ML382 is colored by yellow. **b, c**, Key interactions between the 2-ethoxyphenyl (**b**) and cyclopropyl sulfonamide (**c**) groups of ML382 and the MRGPRX1 receptor. Hydrogen bonds are shown as red dashed lines. **d**, Effects of allosteric pocket mutations on ML382-potentiated BAM8-22 activation. ΔpEC_{50} represents the difference between the pEC_{50} of BAM8-22 and the pEC_{50} of BAM8-22 in the presence of 10 μ M ML382. ND, not determined. Data are mean \pm s.e.m. of $n = 3$

biological replicates. Statistics analyses were performed using one-way ANOVA followed by Dunnett's test. * $P < 0.05$; ** $P < 0.01$; *** $P < 0.001$; **** $P < 0.0001$; NS, no significant difference. (I258A, $P < 0.0001$; L255A, ND; H254A, ND; M102A, $P = 0.2508$; F236A, ND; F232A, ND; Y99A, $P = 0.0014$; Y82A, $P < 0.0001$; R79A, ND; T34A, $P = 0.1924$; T31A, $P = 0.0108$.) **e**, Binding of ML382 leads to a closer interaction of Arg20 with the two acidic residues D177^{5.36} and E157^{4.60}. Sidechain movements of MRGPRX1 are highlighted by red arrows. Hydrogen bonds are shown as red dashed lines. **f**, Conformational changes of allosteric pocket upon ML382 binding.

the cyclopropyl group of ML382 is in direct contact with BAM8-22, modifying the cyclopropyl group with larger chemical moieties could introduce a structural clash with BAM8-22, thereby precluding peptide binding and receptor activation.

To clarify the structural basis of PAM activity, we compared the structure of MRGPRX1 bound to both BAM8-22 and ML382 with the BAM8-22-alone MRGPRX1 structure (Fig. 3e,f and Extended Data Fig. 5a–e). Although the peptide is better resolved in the presence of the allosteric molecule ML382, the superposition of these two models reveals an almost identical overall conformation of the BAM8-22 as well as the intracellular G protein coupling site (Extended Data Fig. 5a–c). However, large conformational changes in both the main-chain helices and the sidechain rotamers of the allosteric pocket are observed. Specifically, seven of the 11 allosteric pocket residues, including T31^{1.36}, R79^{2.57}, Y82^{2.60}, Y99^{3.29}, M102^{3.33}, F236^{6.55} and L255^{7.36}, move outward from their PAM-free state to create an enlarged space for ML382 binding (Fig. 3f and Extended Data Fig. 5d,e). In particular, the aromatic ring of residue Y82^{2.60} is displaced 3 Å upward, and π - π interacts with the benzamide group of ML382, whereas the sidechain of M102^{3.33} moves downward by 2 Å, both accommodating the ML382 benzamide group. Accompanied by these sidechain conformational changes, there is a 1.3-Å outward movement of TM2 and a 1.7-Å inward movement of TM3 (Fig. 3f), respectively, upon ML382 binding. These conformational changes suggest that the allosteric pocket of MRGPRX1 has considerable plasticity, which could provide opportunities for discovering novel BAM8-22 PAM molecules with different chemical scaffolds.

The binding of ML382 to the allosteric pocket also pushes the two bridging residues, Y99^{3.29} and F236^{6.55}, toward the Arg20 of BAM8-22, resulting in a closer charge interaction between Arg20 and the acidic residues D177^{5.36} and E157^{4.60} (Fig. 3e). In addition, the direct contact between ML382 and the BAM8-22 may further increase the peptide affinity at MRGPRX1. In our BRET2 PAM assay, ML382 substantially improves the potency of BAM8-22 (~300-fold in the presence of 30 μ M ML382), whereas the efficacy of the peptide is largely unaffected (Extended Data Fig. 4a and Supplementary Table 2). Indeed, the allosteric effect of ML382 is so strong that it even can rescue the signaling of H254^{7.35}A mutant, which displays no activity in response to BAM8-22 (Extended Data Fig. 4g). Furthermore, ML382 displays weak PAM activity toward the small-molecule agonist compound-16 (Supplementary Fig. 4 and Extended Data Fig. 7d); thus, ML382 exhibits strong probe dependence and is a BAM8-22-specific PAM. A GPCRome screening of ML382 shows that it has no agonist activity at 318 non-olfactory GPCRs, revealing that it has good selectivity for MRGPRX1 (Extended Data Fig. 6a). In the previously determined structures of M2R, GPR40 and DRD1, the PAMs displayed no contact with their corresponding orthosteric agonist (Extended Data Fig. 3b–d)^{23,25,26}. Thus, the direct contact of ML382 with BAM8-22 observed in this study suggests a unique allosteric modulatory mechanism for MRGPRX1.

Binding of compound-16 to MRGPRX1

In recent years, several new ligands that targeted to the MRGPRX1 receptor have been discovered^{17,27,28}. Among these, compound-16 is a highly potent agonist of MRGPRX1 with superior selectivity over

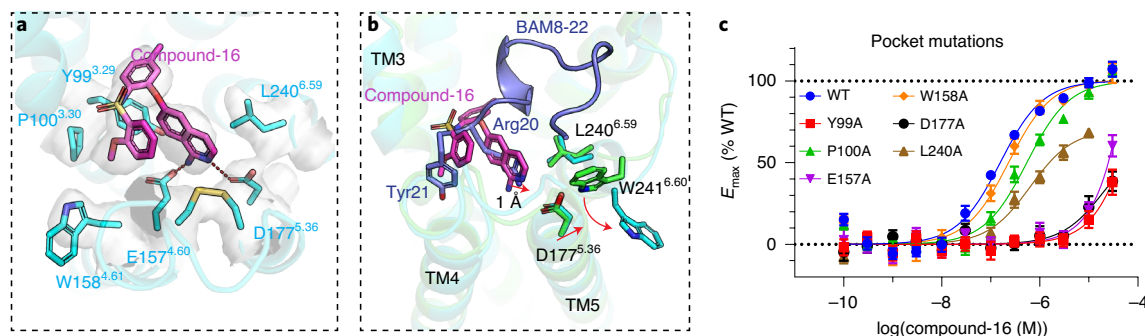


Fig. 4 | Interactions of compound-16 with MRGPRX1 receptor. **a**, Binding pocket of compound-16. Hydrogen bonds are shown as red dashed lines. **b**, Residue W241^{6.60} adopts a different conformation upon binding to compound-16. **c**, BRET2 validation of the compound-16 binding pocket. Data are mean \pm s.e.m. of $n = 3$ biological replicates. E_{\max} , maximum effect; WT, wild-type.

opioid receptors¹⁷, MRGPRX2, MRGPRX4 and many other non-olfactory GPCRs (Extended Data Fig. 6b–h and Supplementary Fig. 5). Moreover, *in vivo* pharmacokinetics studies in mice revealed that compound-16 was preferentially distributed in spinal cord, where its presumed sites for MRGPRX1-mediated analgesic effects reside¹⁷.

Our structure of compound-16-bound MRGPRX1–Gq complex provides a starting point to investigate small-molecule agonism of MRGPRX1. As seen with the peptide agonist BAM8-22, compound-16 also binds shallowly to the orthosteric pocket of MRGPRX1 (Figs. 1f and 4a,b). The aminoisoquinoline group of compound-16 extends toward the two acidic residues and interacts with both D177^{5.36} and E157^{4.60}, further highlighting the importance of charge interactions in MRGPRX1 activation (Fig. 4a). Additionally, the methylphenyl group of compound-16 stacks on the top of Y99^{3.29} through π – π interactions (Fig. 4a). Alanine substitution of Y99^{3.29}, D177^{5.36} and E157^{4.60} greatly reduced the potency of compound-16-stimulated MRGPRX1 activation (Fig. 4c and Supplementary Table 1), suggesting that these residues are important for the agonist activity of compound-16. Lastly, the methoxybenzene group of compound-16 binds into a cavity formed by Y99^{3.29}, P100^{3.30}, E157^{4.60} and W158^{4.61} mainly through hydrophobic interactions.

Compared to BAM8-22, the overall binding mode of compound-16 is similar to that of the C-terminal residues Arg20 and Tyr21 of BAM8-22 (Fig. 4b). However, the large aminoisoquinoline group of compound-16 has a 1.0-Å closer contact with D177^{5.36} than the Arg20 of BAM8-22, which slightly pushes D177^{5.36} toward W241^{6.60}. The movement of D177^{5.36} further leads to a subsequent clash with W241^{6.60} and may finally force W241^{6.60} to rotate outward to the cell membrane (Fig. 4b). Thus, the orthosteric pocket for compound-16 is much larger than that of BAM8-22 (Extended Data Fig. 7a). When aligned with the ML382-bound MRGPRX1–Gq–BAM8-22 structure, compound-16 has a weak contact with the PAM molecule ML382 (Extended Data Fig. 7b,c). This might explain why ML382 only has a mild PAM effect on compound-16-stimulated MRGPRX1 activation (Supplementary Fig. 4 and Extended Data Fig. 7d).

Structural comparisons with MRGPRX2 and MRGPRX4

Although belonging to the same MRGPRX family, MRGPRX1 displays a distinct extracellular pocket compared to MRGPRX2 and MRGPRX4 (Fig. 5a,b). Large conformational differences in the three ECLs as well as the extracellular ends of TM3, TM4 and TM7 are observed (Fig. 5a,b). Of note, the ECL2 and ECL3 of MRGPRX1 move further away from the central axis of receptor, creating a larger pocket for agonist recognition (Fig. 5b,c). In addition, the electrostatic surfaces of MRGPRX1, MRGPRX2 and MRGPRX4 are quite different from each other (Fig. 5d–f). Specifically, MRGPRX1 has a negatively charged orthosteric pocket brought by the two conserved acidic residues D177^{5.36} and E157^{4.60}, whereas its allosteric pocket is positively charged (Fig. 5d).

In MRGPRX2, the orthosteric pocket is also highly negatively charged. However, the sub-pocket 2, which corresponds to the allosteric pocket of MRGPRX1, is relatively hydrophobic (Fig. 5e), whereas, in MRGPRX4, the insertion of ECL2 into the canonical orthosteric pocket made the acidic residues inaccessible, generating a highly positively charged pocket (Fig. 5f). Furthermore, the MRGPRX receptors have variable residue compositions in both the orthosteric and allosteric pockets (Extended Data Fig. 8a–c). This might explain why compound-16 and ML382 showed neither agonist nor allosteric activity to the MRGPRX2 and MRGPRX4 receptors (Supplementary Figs. 5 and 6). Collectively, these observations indicate that MRGPRX receptors have highly different extracellular ligand binding pockets in terms of pocket size, charge distribution and residue composition, indicating that MRGPRX receptors are evolved to respond to different stimuli.

In contrast to the extracellular pocket, MRGPRX1 displays a similar Gq binding mode when compared to that of MRGPRX2 and MRGPRX4 at the intracellular side of the receptor (Fig. 5c)¹⁶. In all the three MRGPRX1–Gq complex structures, the cytoplasmic distance between TM3 and TM6 is approximately 15 Å, which is typically observed from the active state structures of other family A GPCRs^{16,18}. The main interface between MRGPRX1 and the Gq trimer is composed of TM2, TM3, TM5–TM7 and ICL2 of the receptor and the α 5-helix and α N-helix of Gq (Extended Data Fig. 9a,b). Although extensive interactions with the Gq protein were observed, mutagenesis study showed that alanine substitution of most of the MRGPRX1 interface residues have mild effects on agonist-stimulated Gq activation (Extended Data Fig. 9c–e and Supplementary Table 3), and only several ICL2 mutations of MRGPRX1 have relatively large effects on the Gq activation (Extended Data Fig. 9f–h and Supplementary Table 3). Notably, ICL2 of many class A GPCRs binds into a hydrophobic cleft mainly formed by the α N helix, β 2– β 3 loop and α 5 helix. As G protein coupling to GPCRs requires a conformational rearrangement in this region to destabilize its GDP binding pocket before fully coupling²⁹, the large effects of ICL2 mutations observed on MRGPRX1-mediated Gq activation suggest that the interaction between ICL2 and Gq is crucial for the initial process of Gq coupling¹⁶. Notably, the intracellular cavity residues for G protein coupling are highly conserved across MRGPRX family receptors, indicating that they share a conserved downstream signaling pathway.

Discussion

The cryo-EM structures of agonist-bound MRGPRX1–Gq complexes obtained in this study offer important insights into the receptor activation by both the endogenous peptide agonist BAM8-22 and the synthetic small-molecule agonist compound-16. Similarly to MRGPRX2 and MRGPRX4 agonist binding modes, BAM8-22 and compound-16 bind shallowly to the orthosteric pocket of MRGPRX1 (Fig. 1e,f), indicating that this unique ligand binding mode may be general to the

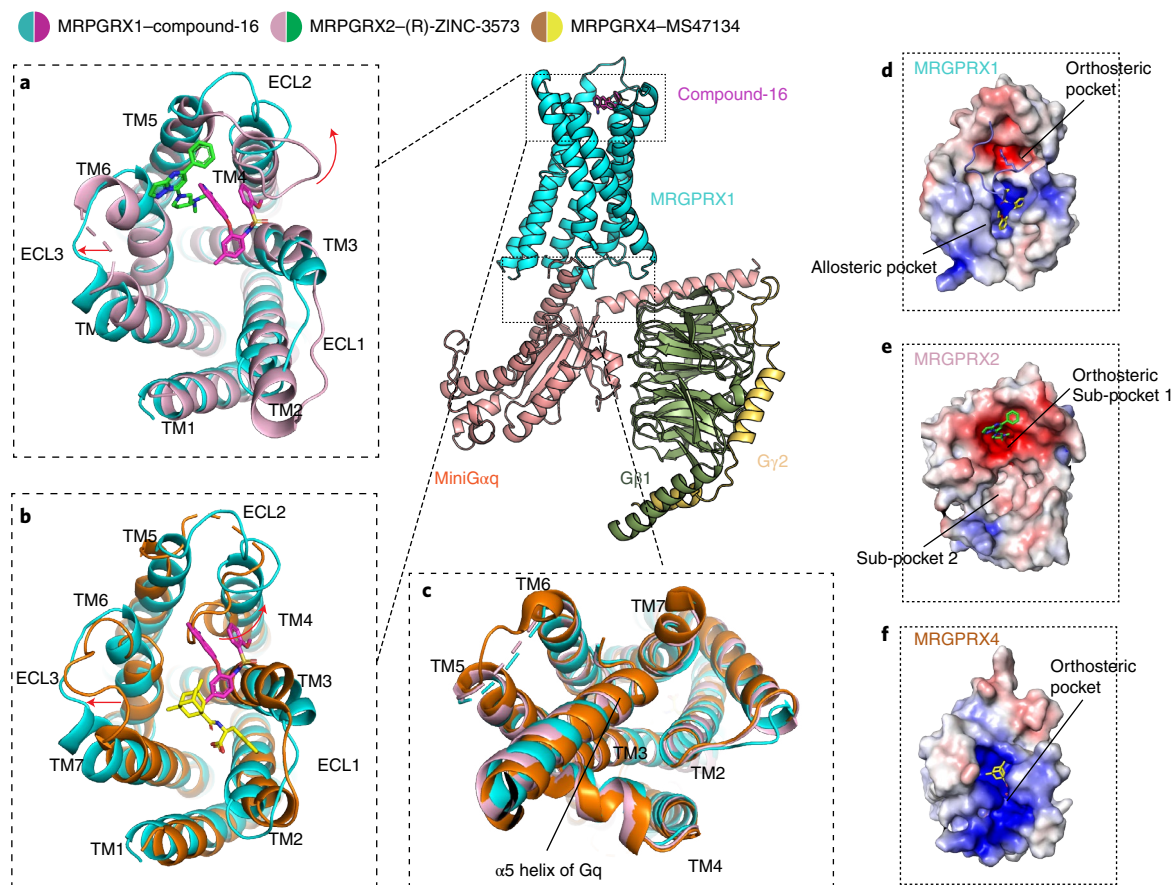


Fig. 5 | Structural comparison of MRGPRX1 with MRGPRX2 and MRGPRX4.

a, Structural comparison of MRGPRX1–compound-16 complex (cyan) with the MRGPRX2–(R)-ZINC3573 complex (PDB: 7S8N; red). Displacements of the extracellular part of MRGPRX1 relative to MRGPRX2 are highlighted with red arrows. Compound-16 (magenta) and (R)-ZINC3573 (green) are shown as sticks. **b**, Structural comparison of MRGPRX1–compound-16 (cyan) complex with the MRGPRX4–MS47134 (PDB: 7S8P; orange) complex. Displacements of the

extracellular part of MRGPRX1 relative to MRGPRX4 are highlighted with red arrows. Compound-16 (magenta) and MS47134 (yellow) are shown as sticks. **c**, MRGPRX1 (cyan) displays a similar intracellular conformation to MRGPRX2 (red) and MRGPRX4 (orange). **d–f**, Electrostatic surface representation of the MRGPRX1 (**d**), MRGPRX2 (**e**) and MRGPRX4 (**f**) extracellular pocket calculated using the APBS plugin in PyMOL. Red, negative (-5 kT e^{-1}); blue, positive ($+5 \text{ kT e}^{-1}$).

MRGPRX family receptors. Additionally, MRGPRX1 also recognizes its agonist through D177^{5,36} and E157^{4,60} (Figs. 2a and 4a), the two conserved acidic residues critical for receptor activation in MRGPRX2. However, due to the structural differences in the orthosteric pocket, MRGPRX1 does not promiscuously bind positively charged peptides. As the two acidic residues also exist in MRGPRX3, it is possible that MRGPRX3 also recognizes some as yet unidentified endogenous peptides containing Arg or Lys if the acidic residues are exposed to the orthosteric pocket. Moreover, the high-resolution structure of ML382-bound MRGPRX1–Gq–BAM8-22 complex also reveals the allosteric modulation mechanism of MRGPRX1. Although we are not able to measure the binding affinity of BAM8-22 due to the lack of radioligand, the direct contact between ML382 and BAM8-22 probably strengthens the binding affinity of BAM8-22 as there is a considerable increase of the BAM8-22 potency with increased concentration of ML382 (Extended Data Fig. 4). We also observed large conformational changes in the ML382 binding site. The structural plasticity of the PAM pocket may provide chances to discover novel PAM molecules with different scaffold and improved pain-relieving effects.

Together with our previously solved structures of MRGPRX2 and MRGPRX4, the MRGPRX structures reveal the general and distinct features of MRGPRX receptors. In contrast to serotonin (5-hydroxytryptamine (5-HT)) receptors, which have a similar 5-HT binding pocket but couple to different G proteins³⁰, the MRGPRX family receptors have a highly conserved G protein coupling interface

but with very different extracellular pockets in the pocket shapes, residue compositions and charge distributions (Fig. 5 and Extended Data Fig. 8), indicating that MRGPRX family receptors respond to different itch or pain stimuli with a common G protein signaling profile. As MRGPRX are primate-exclusive receptors playing important roles in itch and pain signals, it might be useful to study these receptors in an evolutionary perspective when pairing its endogenous agonists.

In summary, the cryo-EM structures of MRGPRX1–Gq complexes obtained in this study offer unique insights into the receptor activation and allosteric modulation of MRGPRX1, which could accelerate the structure-based drug discovery for the non-opioid pain medicines targeting MRGPRX1 as well as the understanding of the diverse ligand recognition profile of MRGPRX family receptors.

Online content

Any methods, additional references, Nature Research reporting summaries, source data, extended data, supplementary information, acknowledgements, peer review information; details of author contributions and competing interests; and statements of data and code availability are available at <https://doi.org/10.1038/s41589-022-01173-6>.

References

1. St Sauver, J. L. et al. Why patients visit their doctors: assessing the most prevalent conditions in a defined American population. *Mayo Clin. Proc.* **88**, 56–67 (2013).

2. Sharif, B., Ase, A. R., Ribeiro-da-Silva, A. & Seguela, P. Differential coding of itch and pain by a subpopulation of primary afferent neurons. *Neuron* **106**, 940–951 (2020).
3. Racine, M., Hudson, M., Baron, M., Nielson, W. R. & Canadian Scleroderma Research, G. The impact of pain and itch on functioning and health-related quality of life in systemic sclerosis: an exploratory study. *J. Pain. Symptom Manag.* **52**, 43–53 (2016).
4. Klein, A. et al. Pruriception and neuronal coding in nociceptor subtypes in human and nonhuman primates. *eLife* **10**, e64506 (2021).
5. Sun, S. et al. Leaky gate model: intensity-dependent coding of pain and itch in the spinal cord. *Neuron* **93**, 840–853 (2017).
6. Shim, W. S. & Oh, U. Histamine-induced itch and its relationship with pain. *Mol. Pain.* **4**, 29 (2008).
7. Meixiong, J. & Dong, X. Mas-related G protein-coupled receptors and the biology of itch sensation. *Annu. Rev. Genet.* **51**, 103–121 (2017).
8. Akiyama, T., Lerner, E. A. & Carstens, E. Protease-activated receptors and itch. *Handb. Exp. Pharmacol.* **226**, 219–235 (2015).
9. Feng, J. et al. Piezo2 channel–Merkel cell signaling modulates the conversion of touch to itch. *Science* **360**, 530–533 (2018).
10. Dong, X., Han, S., Zylka, M. J., Simon, M. I. & Anderson, D. J. A diverse family of GPCRs expressed in specific subsets of nociceptive sensory neurons. *Cell* **106**, 619–632 (2001).
11. Liu, Q. et al. Sensory neuron-specific GPCR Mrgpr8 are itch receptors mediating chloroquine-induced pruritus. *Cell* **139**, 1353–1365 (2009).
12. Li, Z. et al. Targeting human Mas-related G protein-coupled receptor X1 to inhibit persistent pain. *Proc. Natl Acad. Sci. USA* **114**, E1996–E2005 (2017).
13. Lembo, P. M. et al. Proenkephalin A gene products activate a new family of sensory neuron-specific GPCRs. *Nat. Neurosci.* **5**, 201–209 (2002).
14. Wen, W. et al. Discovery and characterization of 2-(cyclopropanesulfonamido)-N-(2-ethoxyphenyl)benzamide, ML382: a potent and selective positive allosteric modulator of MrgX1. *ChemMedChem* **10**, 57–61 (2015).
15. Tseng, P. Y., Zheng, Q., Li, Z. & Dong, X. MrgprX1 mediates neuronal excitability and itch through tetrodotoxin-resistant sodium channels. *Itch (Phila)* **4**, e28 (2019).
16. Cao, C. et al. Structure, function and pharmacology of human itch GPCRs. *Nature* **600**, 170–175 (2021).
17. Prchalová, E. et al. Discovery of benzamidine- and 1-aminoisoquinoline-based human MAS-related G-protein-coupled receptor X1 (MRGPRX1) agonists. *J. Med. Chem.* **62**, 8631–8641 (2019).
18. Kim, K. et al. Structure of a hallucinogen-activated Gq-coupled 5-HT2A serotonin receptor. *Cell* **182**, 1574–1588 (2020).
19. Koehl, A. et al. Structure of the μ -opioid receptor–G_i protein complex. *Nature* **558**, 547–552 (2018).
20. Ballesteros, J. A. & Weinstein, H. in *Methods in Neurosciences* Vol. 25 (ed Sealfon, S. C.) 366–428 (Academic Press, 1995).
21. Han, S. K. et al. Orphan G protein-coupled receptors MrgA1 and MrgC11 are distinctively activated by RF-amide-related peptides through the G $\alpha_{q/11}$ pathway. *Proc. Natl Acad. Sci. USA* **99**, 14740–14745 (2002).
22. Olsen, R. H. J. et al. TRUPATH, an open-source biosensor platform for interrogating the GPCR transducerome. *Nat. Chem. Biol.* **16**, 841–849 (2020).
23. Kruse, A. C. et al. Activation and allosteric modulation of a muscarinic acetylcholine receptor. *Nature* **504**, 101–106 (2013).
24. Wold, E. A., Chen, J., Cunningham, K. A. & Zhou, J. Allosteric modulation of class A GPCRs: targets, agents, and emerging concepts. *J. Med. Chem.* **62**, 88–127 (2019).
25. Lu, J. et al. Structural basis for the cooperative allosteric activation of the free fatty acid receptor GPR40. *Nat. Struct. Mol. Biol.* **24**, 570–577 (2017).
26. Zhuang, Y. et al. Mechanism of dopamine binding and allosteric modulation of the human D1 dopamine receptor. *Cell Res.* **31**, 593–596 (2021).
27. Karhu, T. et al. Isolation of new ligands for orphan receptor MRGPRX1—hemorphins LVV-H7 and VV-H7. *Peptides* **96**, 61–66 (2017).
28. Li, X. et al. Tick peptides evoke itch by activating MrgprC11/MRGPRX1 to sensitize TRPV1 in pruriceptors. *J. Allergy Clin. Immunol.* **147**, 2236–2248 (2021).
29. Du, Y. et al. Assembly of a GPCR-G protein complex. *Cell* **177**, 1232–1242 (2019).
30. Xu, P. et al. Structural insights into the lipid and ligand regulation of serotonin receptors. *Nature* **592**, 469–473 (2021).

Publisher's note Springer Nature remains neutral with regard to jurisdictional claims in published maps and institutional affiliations.

Springer Nature or its licensor holds exclusive rights to this article under a publishing agreement with the author(s) or other rightsholder(s); author self-archiving of the accepted manuscript version of this article is solely governed by the terms of such publishing agreement and applicable law.

© The Author(s), under exclusive licence to Springer Nature America, Inc. 2022

Methods

Generation of MRGPRX1 constructs for cryo-EM and functional assays

For the expression of MRGPRX1–Gαq protein complex, the full-length DNA of human *MRGPRX1* (UniProtKB: [Q96LB2](#)) was subcloned into a modified version of pFastBac1 (Invitrogen) baculovirus expression vector. Specially, the N-terminal of *MRGPRX1* sequence was incorporated with a string of hemagglutinin (HA) signal peptide, followed by a Flag-tag, a 10× His-tag and a TEV protease site. Then, a thermo-stabilized apocytochrome b562RIL (BRIL) and HRV3C protease sites were fused to the N-terminus of MRGPRX1 to facilitate the protein expression and purification. For the Gαq protein, the same mini-Gα_qN heterotrimer construct used for the expression of HT2A–Gq–NBOH complex¹⁸ was introduced to facilitate the formation of receptor complex. For the functional assays, the human *MRGPRX1* gene was cloned into the pcDNA3.1 vector, and mutations were generated using the NEBuilder HiFi DNA Assembly Cloning Kit (New England Biolabs (NEB)). The sequence of primers is provided in Supplementary Table 4. All the constructs and mutations were verified by DNA sequencing.

Expression of MRGPRX1–Gαq protein complex

The recombinant baculovirus containing the MRGPRX1 and mini-Gα_qN heterotrimer were generated using the Bac-to-Bac Baculovirus Expression System (Invitrogen). In brief, the constructs were first transformed into DH₁₀Bac competent cells for generating recombinant bacmid. Then, *Spodoptera frugiperda* (Sf9) insect cells (Expression Systems) were plated into a 12-well plate at a concentration of 5×10^5 cells per well and transfected with 5 μg of purified bacmid to obtain recombinant baculovirus. After 96 hours of incubation, the supernatant was collected as the P0 viral stock and used to generate high-titer baculovirus P1 stock by infection with 40 ml of 2×10^6 Sf9 cells per milliliter and incubation for 72 hours. Viral titers were determined by flow cytometric analysis of Sf9 cells stained with 1:200 diluted gp64-PE monoclonal antibody (Thermo Fisher Scientific). For the expression of the MRGPRX1–Gαq complex, Sf9 cells were grown to a density of 2.0×10^6 cells per milliliter and then co-infected with the baculoviruses of MRGPRX1 and mini-Gα_qN heterotrimer at a multiplicity of infection (MOI) ratio of 3:1.5. After 48 hours of infection, the cells were harvested by centrifugation, washed in HN buffer (10 mM HEPES and 100 mM NaCl, pH 7.5) and stored at –80 °C for future use.

Purification of MRGPRX1–Gαq protein complex

For the purification of MRGPRX1–Gαq protein complex, the Sf9 cell pellets were thawed on ice and resuspended in buffer containing 20 mM HEPES, pH 7.5, 50 mM NaCl, 1 mM MgCl₂ and 3 units of Apyrase (NEB) supplemented with complete Protease Inhibitor Cocktail tablets (Roche). After stirring for 1.5 hours at room temperature, the cell suspension was dounced to homogeneity and subsequently ultracentrifuged at 72,500g (Ti45 rotor, Beckman) for 30 minutes to collect the membrane. After the membrane was solubilized in buffer containing 40 mM HEPES, pH 7.5, 100 mM NaCl, 5% (w/v) glycerol, 0.6% (w/v) lauryl maltose neopentyl glycol (LMNG) and 0.06% (w/v) cholesteryl hemisuccinate (CHS) for 5 hours at 4 °C with 500 μg of scFv16, the solubilized proteins were isolated by another ultracentrifugation at 105,000g (Ti70 rotor, Beckman) for 30 minutes and then incubated with Talon IMAC resin (Clontech) and 20 mM imidazole overnight at 4 °C. On the next day, the resin with immobilized protein complex was collected with a gravity flow column and washed with 25 column volumes of buffer containing 20 mM HEPES, pH 7.5, 100 mM NaCl, 30 mM imidazole, 0.01% (w/v) LMNG, 0.001% (w/v) CHS and 5% glycerol. Then, the protein complex was eluted with the same buffer supplemented with 250 mM imidazole. Released proteins were further concentrated to 0.5 ml and subjected to size-exclusion chromatography on a Superdex 200 10/300 GL Increase column (GE Healthcare) that was pre-equilibrated with 20 mM HEPES, pH 7.5, 100 mM NaCl, 100 μM TCEP, 0.00075% (w/v)

LMNG, 0.00025 (w/v) glyco-diosgenin (GDN) and 0.00075% (w/v) CHS. Peak fractions were pooled and incubated with 15 μl of His-tagged PreScission protease (GenScript) and 2 μl of PNGase F (NEB) at 4 °C overnight to remove the N-terminal BRIL and potential glycosylation. The proteins were concentrated and further purified by size-exclusion chromatography using the same buffer. Peak fractions were pooled and concentrated to 5 mg ml⁻¹. To ensure a full binding of MRGPRX1 ligands, 100 μM compound 16, 100 μM BAM8-22 or 100 μM BAM8-22/ML382 mixture was added to the concentrated sample and incubated on ice for 2 hours before grid-making.

Expression and purification of the scFv16

The expression and purification of scFv16 was performed as previously described¹⁶. In brief, the scFv16 gene was cloned into a modified pFastBac1 vector, expressed from insect Sf9 cells using the baculovirus method and purified by size-exclusion chromatography. Supernatant containing secreted scFv16 was pH balanced to 7.8 by the addition of Tris base powder. Chelating agents were quenched by the addition of 1 mM nickel chloride and 5 mM calcium chloride and stirred for 1 hour at room temperature. The supernatant was collected by centrifugation and incubated with 1 ml of His60 Ni Superflow Resin (Takara) overnight at 4 °C. On the next day, the resin was collected by a gravity flow column and washed with 20 column volumes of buffer containing 20 mM HEPES, pH 7.5, 500 mM NaCl and 10 mM imidazole. After this, elution was performed with the same buffer supplemented with 250 mM imidazole. Finally, the scFv16 protein was purified by size-exclusion chromatography using a Superdex 200 10/300 GL (GE Healthcare). The peak fraction was collected and concentrated to 2 mg ml⁻¹ for future use.

Cryo-EM grid preparation, data collection and three-dimensional reconstruction

For the preparation of the cryo-EM grid, the samples (3.2 μl) were applied individually onto glow-discharged Quantifoil R1.2/1.3 Au300 holey carbon grids (Ted Pella) in a Vitrobot chamber (FEI Vitrobot Mark IV). The Vitrobot chamber was set at 4 °C and 100% humidity with a blot time range from 2.5 seconds to 5 seconds. The grids were flash frozen in a liquid ethane/propane (40/60) mixture and stored in liquid nitrogen for further screening and data collection.

Cryo-EM imaging was performed on a 200 keV G3 Talos Arctica. Micrographs were recorded using a Gatan K3 direct electron detector at a physical pixel size of 0.88 Å. Movies were automatically collected using SerialEM using a multishot array as previously described³¹. Data were collected at an exposure dose rate of -15 electrons per pixel per second as recorded from counting mode. Images were recorded for -2.7 seconds in 60 subframes to give a total exposure dose of -50 electrons per Å². All subsequent classification and refinement steps were performed within cryoSPARC^{32,33} using a previously described workflow¹⁶. In brief, merged curated non-duplicate particles from multiple picking regimes were subjected to multi-reference refinement. This generated a final stack of particles that created a map with respective resolutions as reported in Supplementary Table 5 (by Fourier shell correlation (FSC) using the 0.143-Å cutoff criterion)³⁴ after local contrast transfer function (CTF) refinement and post-processing in cryoSPARC^{32,33}. Alternative post-sharpening was performed on the two half-maps using deepEMhancer³⁵. For more details, see Extended Data Fig. 1 and Supplementary Table 5.

Model building and refinement

For the models of the MRGPRX1–Gq complexes, we used the maps generated from deepEMhancer for further refinement. The structures of the Gq trimer and scFv16 adopted from the MRGPRX2–Gq complex¹⁶ (Protein Data Bank (PDB): [7S8N](#)) and the predicted MRGPRX1 structure from the AlphaFold³⁶ website (<https://www.alpha-fold.ebi.ac.uk>) were docked into the cryo-EM maps using Chimera³⁷.

The models were manually adjusted in Coot³⁸ and then subjected to several rounds of real-space refinement refinement in Phenix³⁹. In the BAM8-22-alone MRGPRX1 structure, residues Pro11–Tyr21 were modeled. In the ML382-bound MRGPRX1 structure, residues Gly9–Tyr21 of BAM8-22 were modeled. For compound-16, GlideEM⁴⁰ docking was used to help model the molecule into the relatively low-resolution map of MRGPRX1–Gq–compound-16 complex (Supplementary Fig. 7). The model statistics were validated using Molprobrity⁴¹. The refinement statistics are provided in Supplementary Table 5. Structure figures were prepared by either Chimera X⁴² or PyMOL (<https://pymol.org/2/>).

BRET assays

G protein dissociation BRET2 assays were performed as previously described with minor modifications⁴³. In brief, HEK293T cells were co-transfected overnight with human MRGPRX1 receptor or mutations, Gαq-RLuc8, Gβ3 and Gy9-GFP2 constructs at a 2:1:2:2 ratio. After 18–24 hours, the transfected cells were seeded into poly-L-lysine-coated 384-well white clear-bottom cell culture plates at a density of 15,000–20,000 cells and incubated with DMEM containing 1% dialyzed FBS, 100 U ml⁻¹ of penicillin and 100 μg ml⁻¹ of streptomycin for another 24 hours. The next day, the medium was aspirated and washed once with 20 μl of assay buffer (1× HBSS, 20 mM HEPES, 0.1% BSA, pH 7.4). Then, 20 μl of drug buffer containing coelenterazine 400a (Nanolight Technology) at 5 μM final concentration was added to each well and incubated for 5 minutes, followed by the addition of 10 μl of 3× designated drug buffer for 5 minutes. Special for the PAM assay, the cells were added with 10 μl of 3× designated final concentrations of ML382 and incubated for 5 minutes at room temperature. Then, 10 μl of 4× final concentrations of BAM8-22, compound-16, cortistatin-14 or nateglinide were added for another 5 minutes. Finally, the plates were read in PHERAstar FSX (BMG Labtech) with a 410-nm (RLuc8-coelenterazine 400a) and a 515-nm (GFP2) emission filter, at 0.6-second integration times. BRET ratio was computed as the ratio of the GFP2 emission to RLuc8 emission. Data were normalized to percentage of wild-type stimulation with indicated reference agonist and analyzed using non-linear regression (log(agonist) versus response) in GraphPad Prism 9.0 to generate the pEC₅₀ and E_{max} values. Data for the PAM assays were transformed to Net BRET and analyzed using the function (Allosteric EC₅₀ shift) to generate the allosteric parameter pK_B.

GPCRome assay

PRESTO-Tango GPCRome assays were performed to interrogate the MRGPRX1 selectivity of ML382 and compound-16 using a previously published procedure⁴⁴ with modifications. In brief, HTLA cells were plated in poly-L-lysine-coated 384-well white plates at a density of 10,000 cells per well and incubated in 40 μl of DMEM containing 1% dialyzed FBS, 100 U ml⁻¹ of penicillin and 100 μg ml⁻¹ of streptomycin for 6 hours. Then, the cells were transfected with 20 ng per well of codon-optimized Tango constructs overnight. On the next day, the cells were treated with 10 μM drugs and incubated for another 24 hours. The medium was removed, and 20 μl per well of diluted BrightGlo was added to determine the luminescence activity. All the plates were counted in a StakMax counter (Molecular Devices). The results were plotted as fold of average basal against individual receptors in GraphPad Prism 9.0 software.

β-arrestin recruitment Tango assay

For the receptors whose activity increased more than three-fold of basal levels obtained in the GPCRome assay, full dose–response Tango arrestin recruitment assays were used as previously described⁴⁴. In brief, HTLA cells were transiently transfected with Tango DNAs overnight. The cells were seeded into poly-L-lysine-coated 384-well white plates (40 μl per well) with complete DMEM supplemented with 1% dialyzed FBS at a density of 10,000 cells per well for 6 hours. Then, 10 μl of different concentrations of 5× tested compound was added overnight.

The next day, all medium and drug solutions were removed, and 20 μl per well of diluted BrightGlo reagent (Promega) was added. After 20 minutes of incubation, the plates were counted using a StakMax counter (Molecular Devices). Results were plotted as percentage of reference ligand against individual receptors in GraphPad Prism 9.0 software. For FXRP4 and MRGPRX1, results were plotted as fold of basal.

Calcium mobilization assay

HEK293T cells were transiently transfected with the plasmid of MRGPRX1 and incubated overnight in DMEM containing 10% FBS, 100 U ml⁻¹ of penicillin and 100 μg ml⁻¹ of streptomycin. For the calcium mobilization assay, the cells were then plated into poly-L-lysine-coated 384-well black plates (40 μl per well) with DMEM supplemented with 1% dialyzed FBS at a density of 15,000 cells per well for another 24 hours. The medium was removed, and cells were loaded with 20 μl per well of 1× FLIPR calcium dye (Molecular Probes) and 2.5 mM probenecid for 1 hour at 37 °C. Then, the cells were treated with 10 μl of 3× different concentrations (0–30 μM) of ML382 in drug buffer (1× HBSS, 20 mM HEPES and 0.1% BSA, pH 7.4) for 15 minutes at room temperature. The baseline was measured for 10 seconds before the addition of 4× concentrated agonist ligands in drug buffer. Fluorescence was measured for 120 seconds, and data were analyzed in GraphPad Prism 9.0 software.

ELISA

To measure the surface expression level of MRGPRX1 and its mutants, the transfected cells were seeded into 384-well white plates and incubated at 37 °C for 24 hours. The cells were fixed with 4% (v/v) paraformaldehyde for 20 minutes at room temperature and washed twice with PBS. Then, the cells were blocked with 5% (v/v) BSA for 1 hour and further probed with 1:10,000 diluted anti-Flag horseradish peroxidase-conjugated antibody (Sigma-Aldrich, A8592) for another 1 hour. Finally, 20 μl per well of Super Signal ELISA pico chemiluminescent substrate (Thermo Fisher Scientific, 37069) was added, and the luminescence signal was counted using a Wallac TriLux Microbeta counter (PerkinElmer). The data were analyzed in GraphPad Prism 9.0 and normalized to the signal of wild-type MRGPRX1 (Supplementary Fig. 8).

Reporting summary

Further information on research design is available in the Nature Research Reporting Summary linked to this article.

Data availability

The coordinate and cryo-EM map of MRGPRX1–Gq–BAM8-22, MRGPRX1–Gq–BAM8-22/ML382 and MRGPRX1–Gq–compound-16 have been deposited to the Protein Data Bank (Electron Microscopy Data Bank) database with accession codes 8DWC (EMD-27752), 8DWG (EMD-27753) and 8DWH (EMD-27754), respectively. The cryo-EM micrographs of MRGPRX1–Gq–BAM8-22, MRGPRX1–Gq–BAM8-22/ML382 and MRGPRX1–Gq–compound-16 have been deposited in the EMPIAR database (<https://www.ebi.ac.uk/empiar/>) with accession numbers EMPIAR-11183, EMPIAR-11188 and EMPIAR-11191, respectively. Source data are provided with this paper.

References

- Peck, J. V., Fay, J. F. & Strauss, J. D. High-speed high-resolution data collection on a 200 keV cryo-TEM. *IUCr J* **9**, 243–252 (2022).
- Punjani, A., Rubinstein, J. L., Fleet, D. J. & Brubaker, M. A. cryoSPARC: algorithms for rapid unsupervised cryo-EM structure determination. *Nat. Methods* **14**, 290–296 (2017).
- Punjani, A., Zhang, H. & Fleet, D. J. Non-uniform refinement: adaptive regularization improves single-particle cryo-EM reconstruction. *Nat. Methods* **17**, 1214–1221 (2020).
- Rosenthal, P. B. & Henderson, R. Optimal determination of particle orientation, absolute hand, and contrast loss in single-particle electron cryomicroscopy. *J. Mol. Biol.* **333**, 721–745 (2003).

35. Sanchez-Garcia, R. et al. DeepEMhancer: a deep learning solution for cryo-EM volume post-processing. *Commun. Biol.* **4**, 874 (2021).
36. Jumper, J. et al. Highly accurate protein structure prediction with AlphaFold. *Nature* **596**, 583–589 (2021).
37. Pettersen, E. F. et al. UCSF Chimera—a visualization system for exploratory research and analysis. *J. Comput. Chem.* **25**, 1605–1612 (2004).
38. Emsley, P. & Cowtan, K. Coot: model-building tools for molecular graphics. *Acta Crystallogr. D Biol. Crystallogr.* **60**, 2126–2132 (2004).
39. Adams, P. D. et al. PHENIX: a comprehensive Python-based system for macromolecular structure solution. *Acta Crystallogr. D Biol. Crystallogr.* **66**, 213–221 (2010).
40. Robertson, M. J., van Zundert, G. C. P., Borrelli, K. & Skiniotis, G. GemSpot: a pipeline for robust modeling of ligands into cryo-EM maps. *Structure* **28**, 707–716 (2020).
41. Chen, V. B. et al. MolProbity: all-atom structure validation for macromolecular crystallography. *Acta Crystallogr. D Biol. Crystallogr.* **66**, 12–21 (2010).
42. Pettersen, E. F. et al. UCSF ChimeraX: structure visualization for researchers, educators, and developers. *Protein Sci.* **30**, 70–82 (2021).
43. Pryce, K. D. et al. A promising chemical series of positive allosteric modulators of the mu-opioid receptor that enhance the antinociceptive efficacy of opioids but not their adverse effects. *Neuropharmacology* **195**, 108673 (2021).
44. Sadybekov, A. A. et al. Synthon-based ligand discovery in virtual libraries of over 11 billion compounds. *Nature* **601**, 452–459 (2022).
45. Robert, X. & Gouet, P. Deciphering key features in protein structures with the new ENDscript server. *Nucleic Acids Res.* **42**, W320–324 (2014).

Acknowledgements

This work was supported by National Institutes of Health grants R01DA055656 and U24DK116195 to B.L.R. and B.K.S. as well as the Michael Hooker Distinguished Professorship to B.L.R. We thank J. Peck and J. Strauss of the University of North Carolina Cryo-EM Core Facility for their technical assistance with this project.

Author contributions

Y.L. designed the experiments, generated the MRGPRX1 constructs for Sf9 insect cell expression, expressed and purified the MRGPRX1 signaling complexes for cryo-EM study, performed the BRET assays, analyzed the data, prepared the figures and tables and assisted in manuscript preparation. C.C. designed the experiments, assisted in the protein purification, built the models, refined the structures, analyzed the data and prepared the figures and the manuscript. J.F. prepared the cryo-EM grids, collected the cryo-EM data and performed the cryo-EM map calculation. R.H.G. and M.M.R. assisted in the validation of structures. X.-P.H. and Y.L. performed the GPCRome assays. S.-L.S. and Y.L. generated the MRGPRX1 mutations for functional assays. B.E.K designed the mini-Gaq protein construct and assisted in the functional data analysis. S.Z. assisted in the protein expression. B.K.S. provided valuable insights and edited the manuscript. B.L.R. supervised the overall project and edited the manuscript.

Competing interests

The authors declare no competing interests.

Additional information

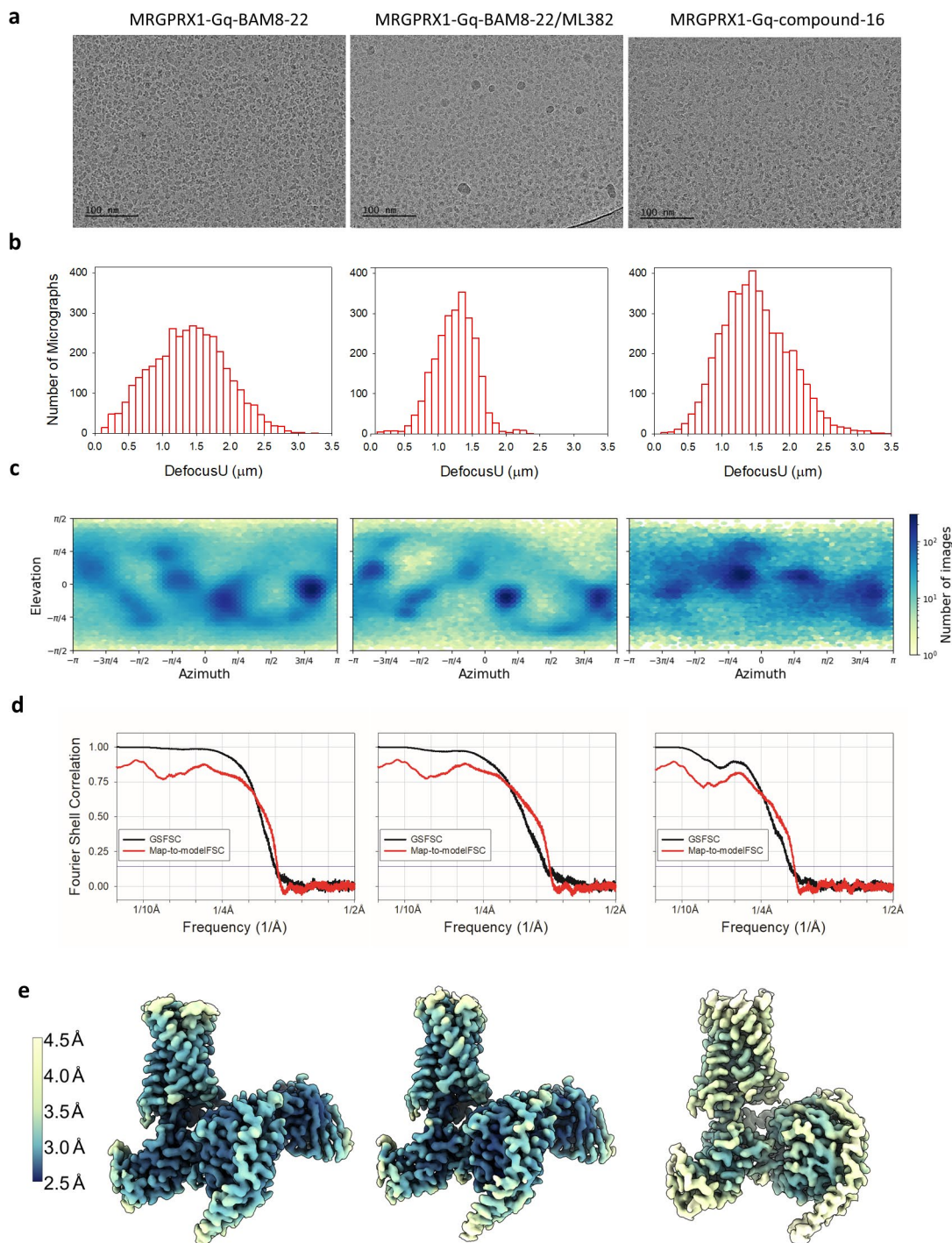
Extended data is available for this paper at <https://doi.org/10.1038/s41589-022-01173-6>.

Supplementary information The online version contains supplementary material available at <https://doi.org/10.1038/s41589-022-01173-6>.

Correspondence and requests for materials should be addressed to Jonathan F. Fay or Bryan L. Roth.

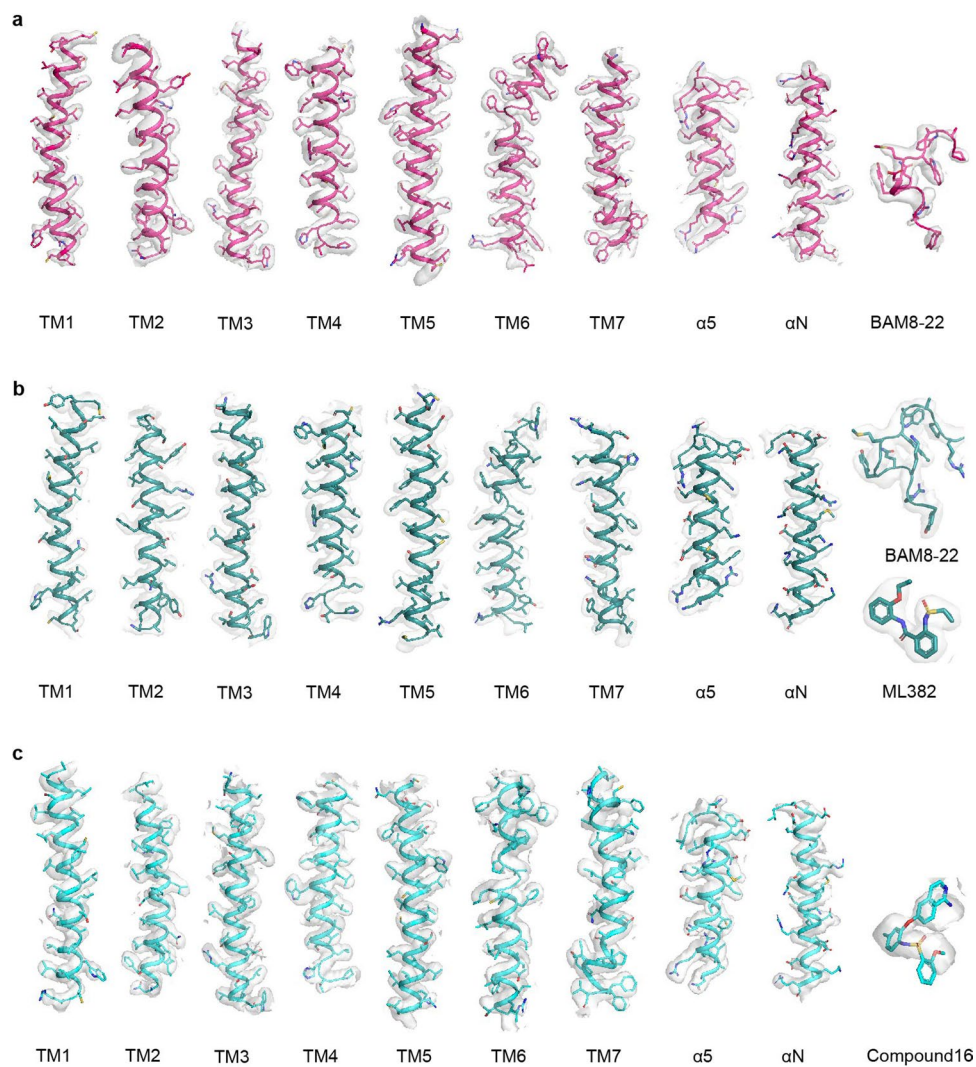
Peer review information *Nature Chemical Biology* thanks Corey Hopkins and the other, anonymous, reviewer(s) for their contribution to the peer review of this work.

Reprints and permissions information is available at www.nature.com/reprints.

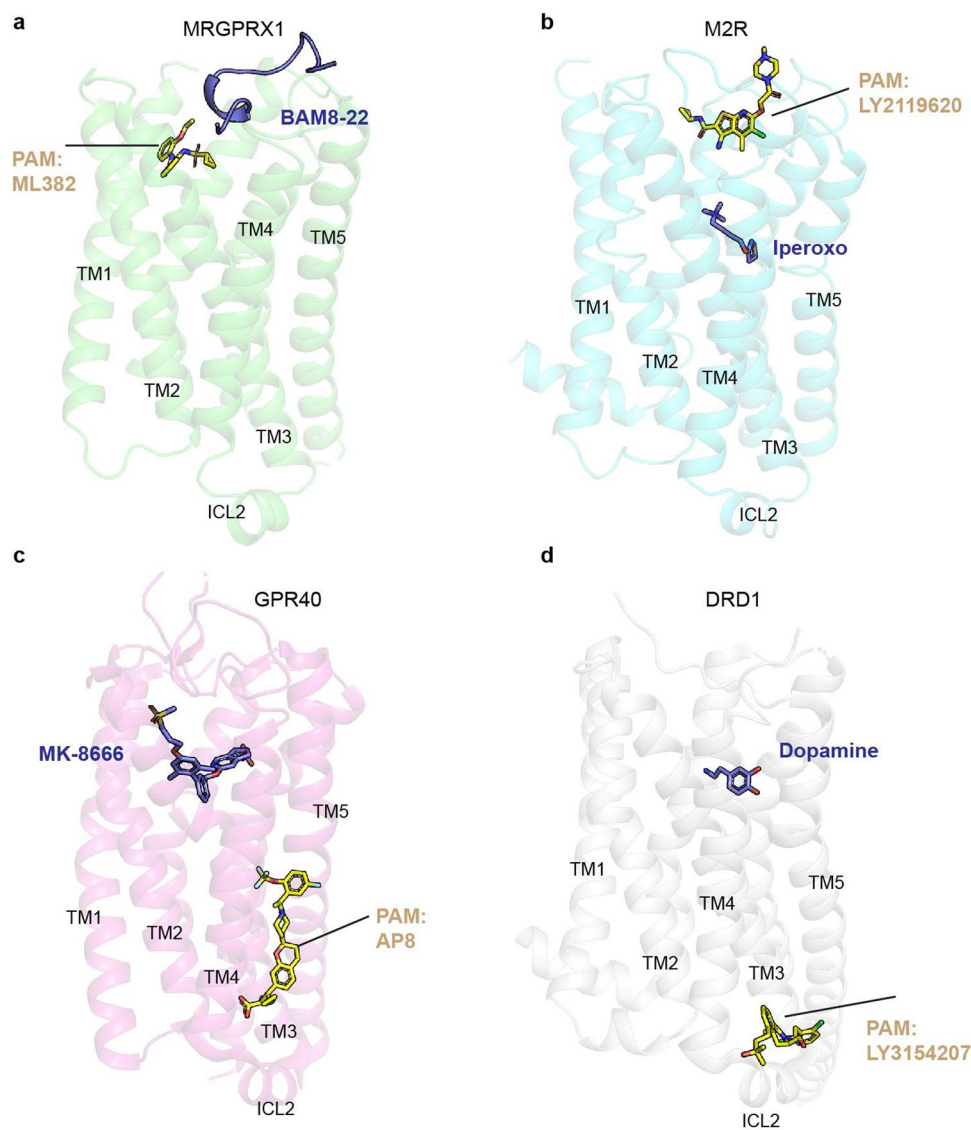


Extended Data Fig. 1 | Extended cryo-EM analysis of the MRGPRX1-Gq complex bound to BAM8-22, BAM8-22/ML382, and compound-16, respectively. **a**, Representative cryo-EM micrograph (scale bar: 100 nm) of the MRGPRX1-Gq-BAM8-22, MRGPRX1-Gq-BAM8-22/ML382 and MRGPRX1-Gq-compound-16 complexes. The exact number of movies and particles used for each complex are shown in Supplementary Fig. 2. The experiment was repeated three times with similar result. **b**, Histograms of defocus values for micrographs

used in the single particle analysis (see Supplementary Table 4 for more details). **c**, Orientational distribution heat map. **d**, 2D plots of the gold standard Fourier shell correlation (GSFSC) between half maps (black) and FSC between model and the B-factor sharpened map for respective refined model (red) as calculated by phenix.mtirage. **e**, Local resolution heat-map calculated using the local windowed FSC method.

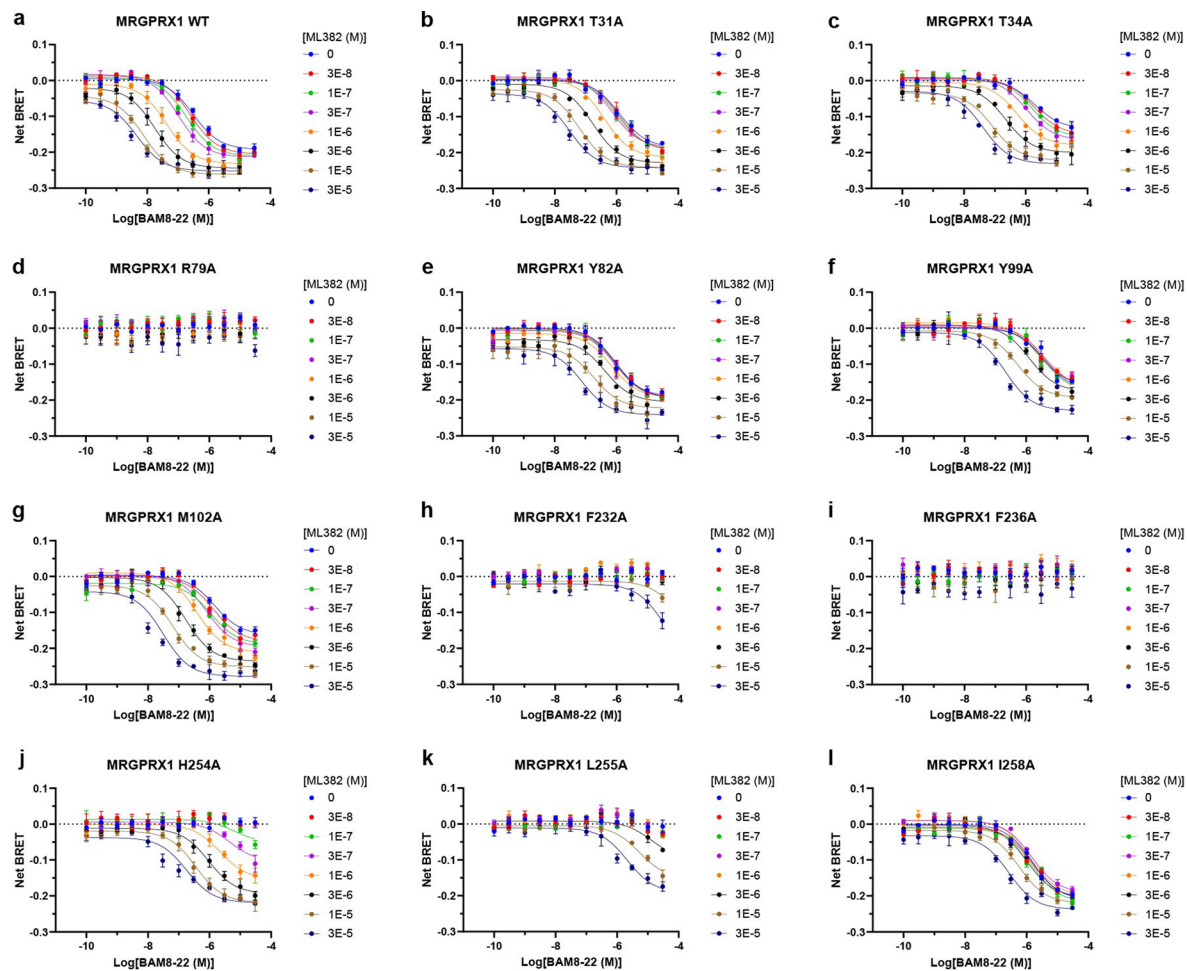


Extended Data Fig. 2 | Electron microscopy density map of MRGPRX1-Gq-BAM8-22, MRGPRX1-Gq-BAM8-22/ML382, and MRGPRX1-Gq-compound-16 complexes. a-c, EM density of the ligand, TM1-TM7 helices of MRGPRX1 and the α5 and αN helices of Gq of MRGPRX1-Gq-BAM8-22 (a), MRGPRX1-Gq-BAM8-22/ML382 (b) and MRGPRX1-Gq-compound-16 (c), respectively.

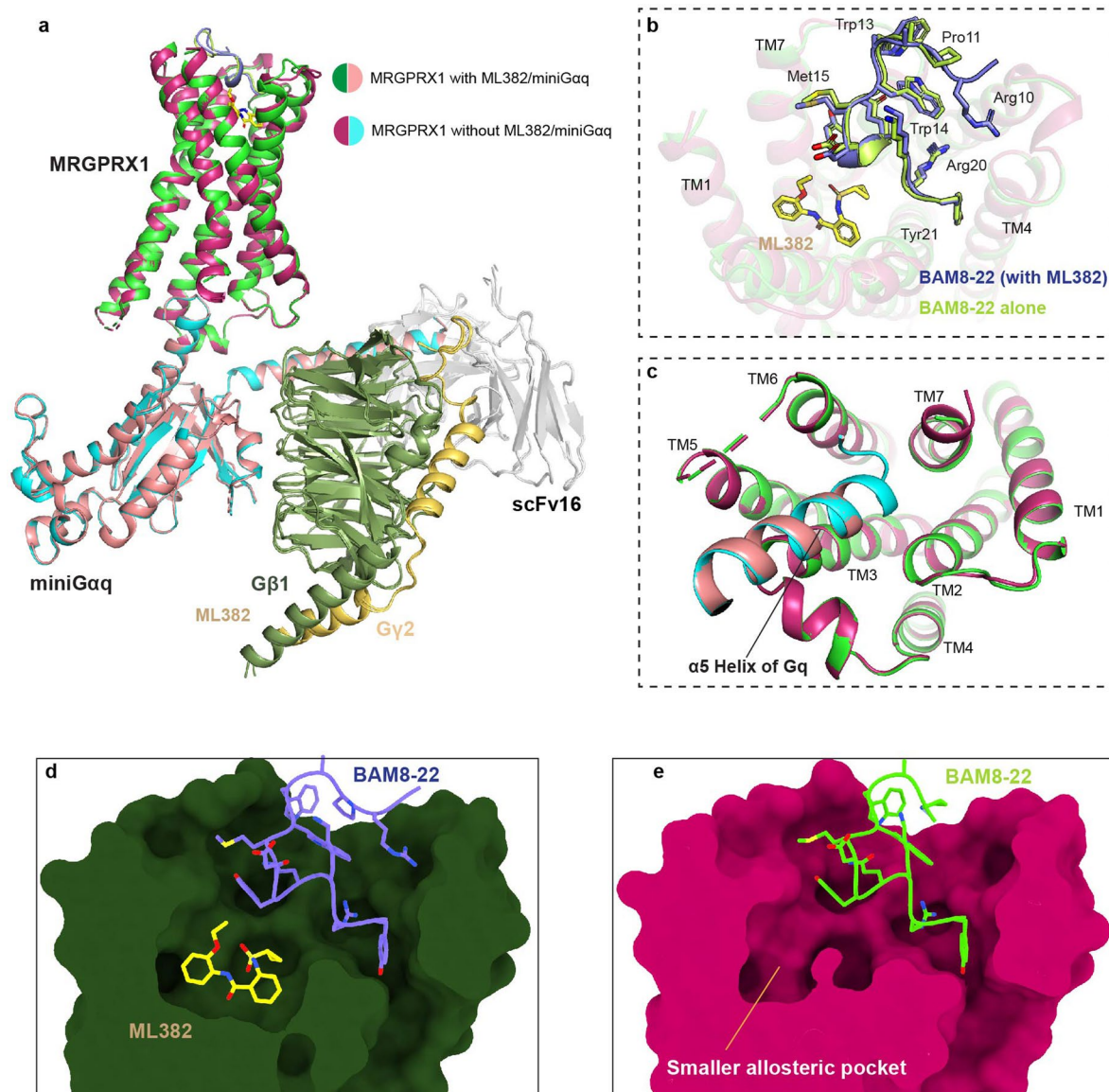


Extended Data Fig. 3 | Comparison of MRGPRX1 PAM binding site with other GPCRs. a-d. The binding modes of agonist and PAM of MRGPRX1 (a), M2R (PDB ID: [4MQT](#)) (b), GPR40 (PDB ID: [5TZY](#)) (c) and DRD1 (PDB ID: [7LJD](#)) (d). The peptide

agonist is shown as cartoon. Small molecule orthosteric agonists and PAMs are shown as sticks. Orthosteric agonist and PAM are colored by blue and yellow, respectively.

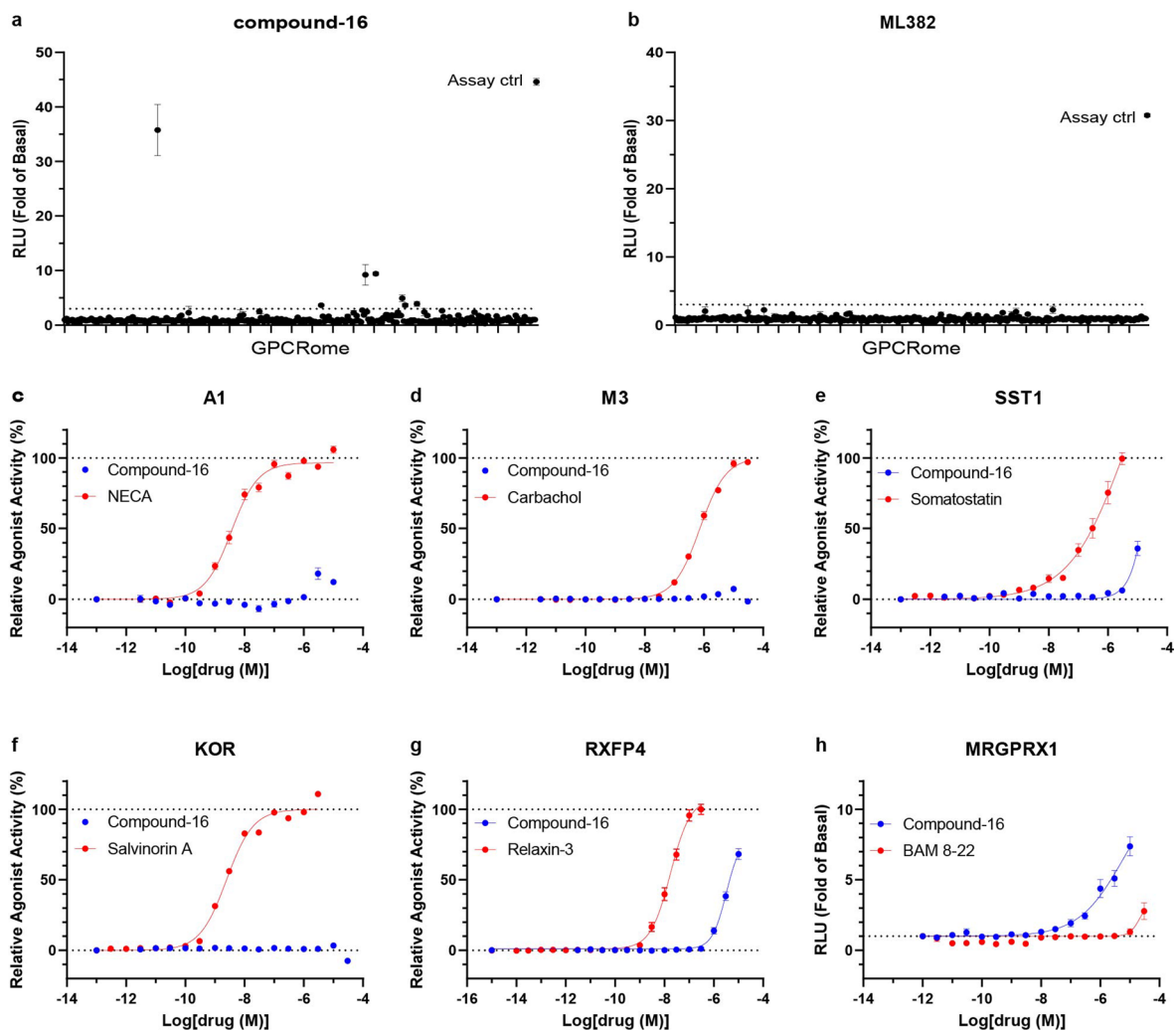


Extended Data Fig. 4 | Mutations of MRGPRX1 allosteric site residues affect ML382 allosteric properties. a-l. Representative Gq BRET2 dose-response curves of WT and mutations of key residues of MRGPRX1 in the presence of indicated concentration of the allosteric modulator ML382. Data are mean \pm SEM of n = 3 biological replicates.



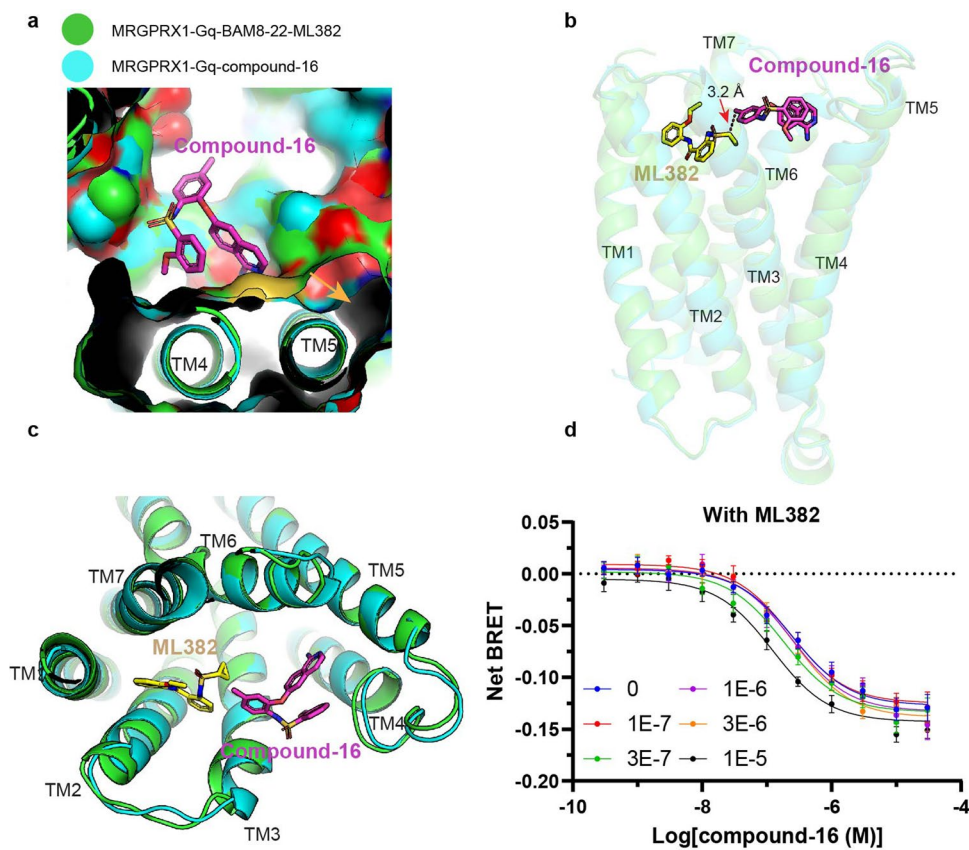
Extended Data Fig. 5 | Structural comparison of the MRGPRX1-Gq-BAM8-22 complex with MRGPRX1-Gq-BAM8-22/ML382 complex. a-c, The overall alignment of the MRGPRX1-Gq-BAM8-22 complex with MRGPRX1-Gq-BAM8-22/ML382 complex. Side-view to show the overall complexes (a). Extracellular view

to show the overall similar peptide binding mode (b). Intracellular view to show the $\alpha 5$ binding pocket (c). d, Cross-section image to show the binding of BAM8-22 and ML382 in MRGPRX1. e, Cross-section image to show the binding of BAM8-22 alone in MRGPRX1.



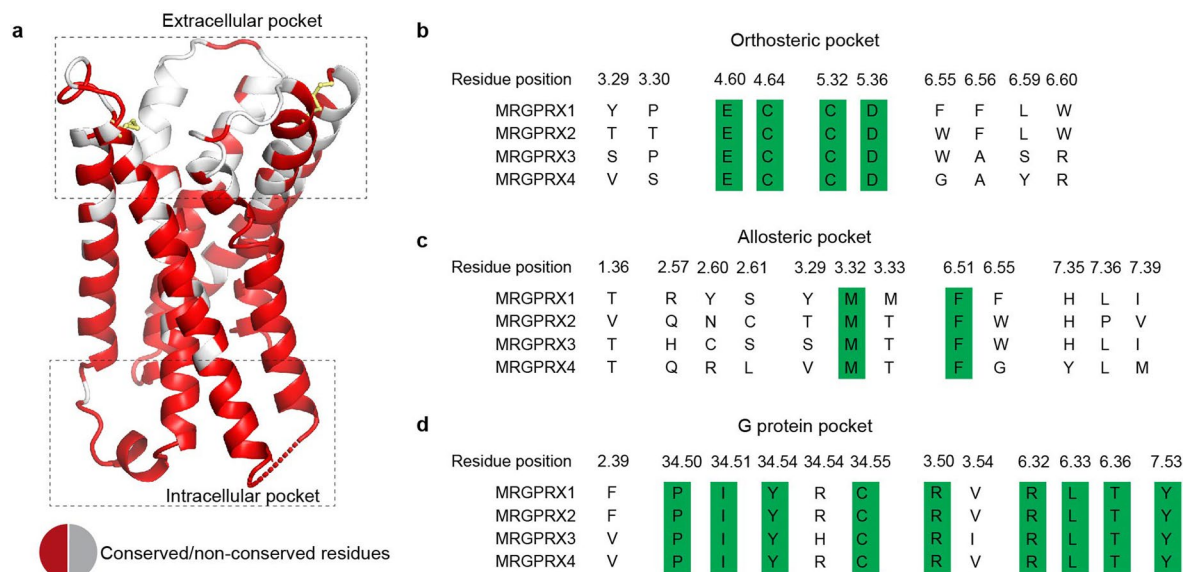
Extended Data Fig. 6 | Selectivity of compound-16 and ML382 among other GPCRs. a-b, Screening of ML382 (**a**) and compound-16 (**b**) in single concentration (10 μ M) at 318 receptors in PRESTO-Tango GPCRome assays. Dopamine (D2) with 100 nM quinpirole was used as the assay control (assay ctrl). The data are plotted as fold of basal activity and presented as mean \pm SEM ($n = 4$). The ones with

>3-fold of basal were taken as pronounced hits. **c-h**, Follow-up dose response curves for the targets with > 3-fold increased activity. Known agonist for each receptor was used as positive controls, and all the results were normalized to these controls (**c-g**). For MRGPRX1, the results were plotted as fold of basal (**g-h**). All the data are presented as mean \pm SEM of $n = 3$ independent experiments.



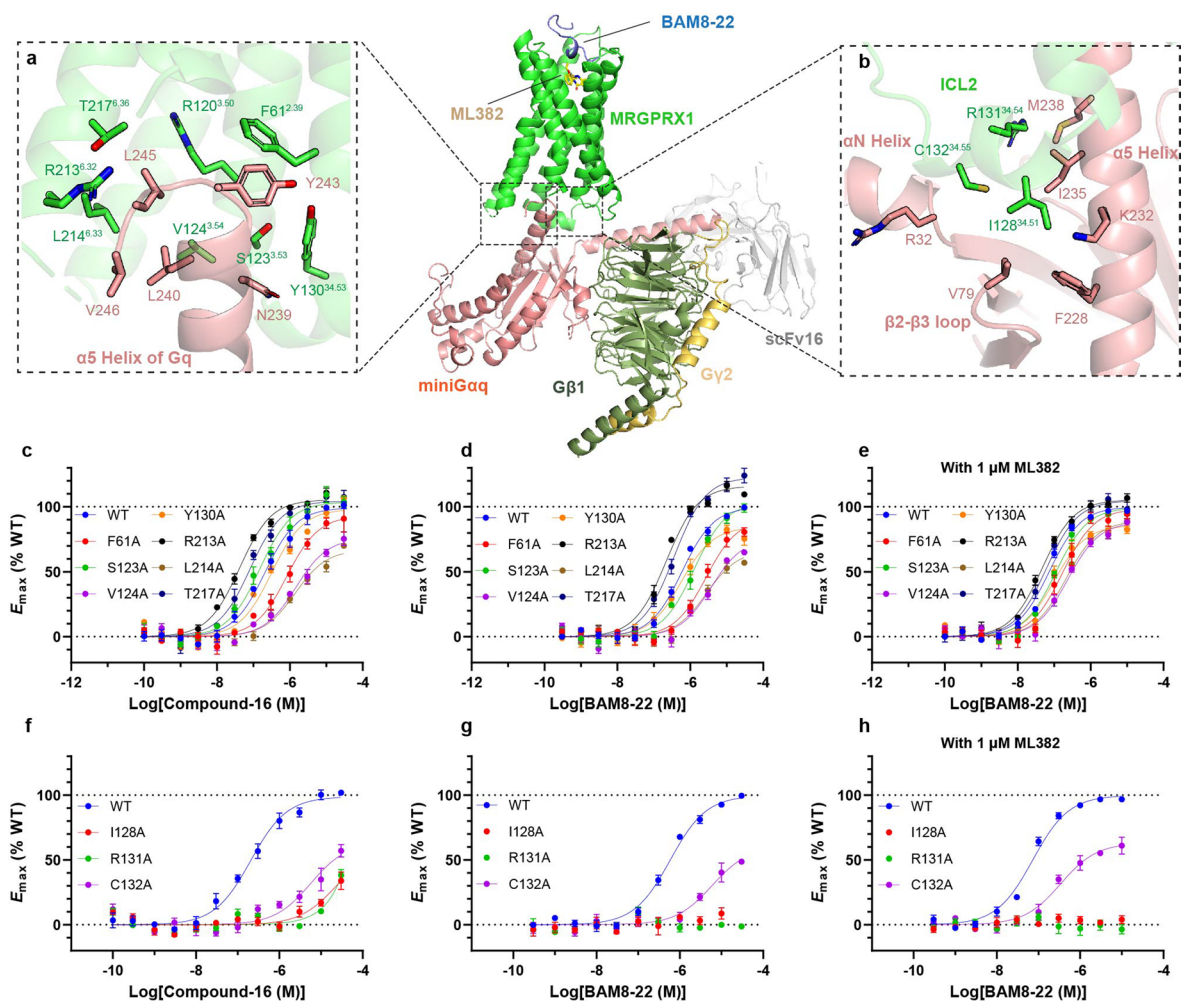
Extended Data Fig. 7 | Structural comparison of MRGPRX1-Gq-compound-16 complex with MRGPRX1-Gq-BAM8-22/ML382 complex. **a**, The orthosteric pocket for compound-16 (cyan) is larger than that of BAM8-22 (green). **b-c**, Structural superposition of MRGPRX1-Gq-compound-16 complex and MRGPRX1-

Gq-BAM8-22/ML382 to show compound-16 has a weak contact with the allosteric modulator ML382. Side view (**b**). Top view (**c**). **d**, ML382 displays very weak PAM activity at compound-16 in BRET2 Gq activation assay. Data are mean \pm SEM of $n = 4$ biological replicates.



Extended Data Fig. 8 | Residue compositions of the extracellular and intracellular pockets of MRGPRX family receptors. a, Structure of MRGPRX1 with the residues conserved in MRGPRX1, MRGPRX2 (PDB: 7S8N) and MRGPRX4 (PDB: 7S8P) colored in red. Figure is generated by ENDscript⁴⁵. **b-d**, Residue

compositions of the orthosteric pocket (**b**), allosteric pocket (**c**) and G protein interface (**d**) of the MRGPRX family receptors. The pocket residues are selected based on the MRGPRX1-Gq-BAM8-22/ML382 structure. The conserved residues are highlighted in green.



Extended Data Fig. 9 | The G protein interface of MRGPRX1. a, key interactions between the intracellular cavity of MRGPRX1 (green) and the $\alpha 5$ helix of Gq (red). The structure of MRGPRX1-Gq-BAM8-22/ML382 complex is used for structural analysis. **b**, Key interactions between the ICL2 of MRGPRX1 and the G protein. **c-e**, BRET2 validation of the intracavity mutations of MRGPRX1 in presence of

compound-16 (**c**), BAM8-22 alone (**d**) and BAM8-22 with 1 μ M ML382 (**e**). **f-h**, BRET2 validation of the ICL2 mutations of MRGPRX1 in presence of compound-16 (**f**), BAM8-22 alone (**g**) and BAM8-22 with 1 μ M ML382 (**h**). Data are mean \pm SEM of $n = 4$ biological replicates.

Reporting Summary

Nature Research wishes to improve the reproducibility of the work that we publish. This form provides structure for consistency and transparency in reporting. For further information on Nature Research policies, see our [Editorial Policies](#) and the [Editorial Policy Checklist](#).

Statistics

For all statistical analyses, confirm that the following items are present in the figure legend, table legend, main text, or Methods section.

n/a Confirmed

- The exact sample size (n) for each experimental group/condition, given as a discrete number and unit of measurement
- A statement on whether measurements were taken from distinct samples or whether the same sample was measured repeatedly
- The statistical test(s) used AND whether they are one- or two-sided
Only common tests should be described solely by name; describe more complex techniques in the Methods section.
- A description of all covariates tested
- A description of any assumptions or corrections, such as tests of normality and adjustment for multiple comparisons
- A full description of the statistical parameters including central tendency (e.g. means) or other basic estimates (e.g. regression coefficient) AND variation (e.g. standard deviation) or associated estimates of uncertainty (e.g. confidence intervals)
- For null hypothesis testing, the test statistic (e.g. F , t , r) with confidence intervals, effect sizes, degrees of freedom and P value noted
Give P values as exact values whenever suitable.
- For Bayesian analysis, information on the choice of priors and Markov chain Monte Carlo settings
- For hierarchical and complex designs, identification of the appropriate level for tests and full reporting of outcomes
- Estimates of effect sizes (e.g. Cohen's d , Pearson's r), indicating how they were calculated

Our web collection on [statistics for biologists](#) contains articles on many of the points above.

Software and code

Policy information about [availability of computer code](#)

Data collection

Data analysis

For manuscripts utilizing custom algorithms or software that are central to the research but not yet described in published literature, software must be made available to editors and reviewers. We strongly encourage code deposition in a community repository (e.g. GitHub). See the Nature Research [guidelines for submitting code & software](#) for further information.

Data

Policy information about [availability of data](#)

All manuscripts must include a [data availability statement](#). This statement should provide the following information, where applicable:

- Accession codes, unique identifiers, or web links for publicly available datasets
- A list of figures that have associated raw data
- A description of any restrictions on data availability

The coordinate and cryo-EM map of MRGPRX1-Gq-BAM8-22, MRGPRX1-Gq-BAM8-22/ML382, and MRGPRX1-Gq-compound-16 have been deposited to PDB (EMDB) database with accession codes 8DWC (EMD-27752), 8DWG (EMD-27753), and 8DWH (EMD-27754), respectively. The cryo-EM micrographs of MRGPRX1-Gq-BAM8-22, MRGPRX1-Gq-BAM8-22/ML382, and MRGPRX1-Gq-compound-16 have been deposited in the EMPIAR database (<https://www.ebi.ac.uk/empiar/>) with accession numbers EMPIAR-11183, EMPIAR-11188, and EMPIAR-11191, respectively. The amino acid sequence of MRGPRX1 could be accessed from UniProtKB (Q96LB2). The source data are provided with this paper.

Field-specific reporting

Please select the one below that is the best fit for your research. If you are not sure, read the appropriate sections before making your selection.

Life sciences Behavioural & social sciences Ecological, evolutionary & environmental sciences

For a reference copy of the document with all sections, see [nature.com/documents/nr-reporting-summary-flat.pdf](https://www.nature.com/documents/nr-reporting-summary-flat.pdf)

Life sciences study design

All studies must disclose on these points even when the disclosure is negative.

Sample size	For cryoEM studies, the number of micrographs is determined by the available microscope time. For Tango, calcium mobilization, BRET and ELISA assays, number of biological replicates were reported in the figure legends. For the time-consuming and labor-intensive GPCRome assay for 318 GPCRs, one biologically independent experiment was performed with n=4 technical replicates. Only initial positive hits from GPCRome were then replicated in subsequent dose-response assay with three biologically independent experiments (n=3). Within this study, the sample size was determined based on variability of the response deviating from the mean as indicated by the standard error of the mean (SEM), which is also presented in the figures. Typically, at least three biological replicates were performed so that the SEM was within at least 20 % of the mean, and exact number of replicates are indicated in figure legends.
Data exclusions	No data were excluded.
Replication	For the GPCRome assay, one biological experiment was performed with n=4 technical replicates. Other experiments were reproduced at least three biologically independent experiments. All attempts at replication were successful.
Randomization	Randomization was not relevant for this study, as the independent variables to be tested were sufficient for the functional interpretation within this study.
Blinding	No blinding was performed in this study. As blinding is not necessary for both cryoEM structure determination and functional studies due to the nature of these experiments do not require subject assessment of the data that may influence the validity of the results.

Reporting for specific materials, systems and methods

We require information from authors about some types of materials, experimental systems and methods used in many studies. Here, indicate whether each material, system or method listed is relevant to your study. If you are not sure if a list item applies to your research, read the appropriate section before selecting a response.

Materials & experimental systems

n/a	Involved in the study
<input type="checkbox"/>	<input checked="" type="checkbox"/> Antibodies
<input type="checkbox"/>	<input checked="" type="checkbox"/> Eukaryotic cell lines
<input checked="" type="checkbox"/>	<input type="checkbox"/> Palaeontology and archaeology
<input checked="" type="checkbox"/>	<input type="checkbox"/> Animals and other organisms
<input checked="" type="checkbox"/>	<input type="checkbox"/> Human research participants
<input checked="" type="checkbox"/>	<input type="checkbox"/> Clinical data
<input checked="" type="checkbox"/>	<input type="checkbox"/> Dual use research of concern

Methods

n/a	Involved in the study
<input checked="" type="checkbox"/>	<input type="checkbox"/> ChIP-seq
<input checked="" type="checkbox"/>	<input type="checkbox"/> Flow cytometry
<input checked="" type="checkbox"/>	<input type="checkbox"/> MRI-based neuroimaging

Antibodies

Antibodies used	The gp64-PE monoclonal antibody was purchased from ThermoFisher (12-6991-82) and used in a 1:200 dilution. The mouse monoclonal ANTI-FLAG horseradish peroxidase conjugated antibody was purchased from Sigma Aldrich (A8592) and used in 1:10,000 dilution. The G protein stabilizing antibody scFv16 was expressed and purified by our lab as indicated in the Methods section of the manuscript. scFv16 was used in 1:1,000 dilution.
Validation	The gp64-PE (R-PHYCOERYTHRIN (R-PE)-conjugated mouse anti-baculovirus monoclonal antibody is from mouse clone AcV1 and used for baculovirus titration. Detailed information can be found at: https://expressionsystems.com/product/gp64-pe-antibody/ . The monoclonal ANTI-FLAG horseradish peroxidase conjugated antibody is from mouse clone M2 and used for measuring protein expression on the surface of cells. Detailed information can be found at: https://www.sigmaaldrich.com/US/en/product/sigma/a8592 . The G protein stabilizing antibody scFv16 was validated by our structural determination cryo-EM experiments.

Eukaryotic cell lines

Policy information about [cell lines](#)

Cell line source(s)	The Sf9 insect cells were purchased from Expression Systems (94-001S). HEK293T cells were purchased from the American Type Culture Collection (ATCC, ATCC CRL-11268). HTLA cells were a gift from R. Axel (Columbia University) .
Authentication	The Sf9 insect cell line is commercial available and obtained from vendor as indicated in the manuscript. HEK293T cells were authenticated by the supplier (ATCC) using morphology and growth characteristics, and STR profiling. HTLA cells (a HEK293 cell line stably expressing a tTA-dependent luciferase reporter and a β -arrestin2-TEV fusion gene) were a gift from R. Axel and was authenticated by morphology, growth characteristics and the successful tango assay which demonstrates that both tTA-dependent luciferase reporter and a β -arrestin2-TEV fusion gene are presented in the cells.
Mycoplasma contamination	Sf9 cell line was certified as Mycoplasma-free by the vendor (Expression Systems). HEK293T cells have been tested and shown to be free from mycoplasma (Hoechst DNA stain and Direct Culture methods employed). HTLA cells were not in particular tested for mycoplasma contamination.
Commonly misidentified lines (See ICLAC register)	None